Experimental modelling of primary migration in a layered, brittle analogue system

James Ronald Johnson [a,*], Maya Kobchenko [a], Andrew Charles Johnson [b], Nazmul Haque Mondol [a,c], François Renard [a,d]

[a] *Department of Geosciences, The Njord Centre, University of Oslo, P.O. Box 1048, Blindern, NO-0316 Oslo, Norway*
[b] *Subsurface Characterization and Reservoir Engineering Unit, SM Energy, 1775 Sherman St., CO 80203, USA*
[c] *Norwegian Geotechnical Institute (NGI), P.O. Box 3930, Ullevaal Stadion, NO-0806 Oslo, Norway*
[d] *ISTerre, Univ. Grenoble Alpes, Grenoble INP, Univ. Savoie Mont Blanc, CNRS, IRD, Univ. Gustave Eiffel, 38000 Grenoble, France*

ARTICLE INFO

ABSTRACT

A 2D Hele-Shaw cell was built to study microfracture nucleation, growth, and network formation during internal fluid production. Fluid is slowly produced into a low permeability solid, which leads to a local fluid pressure increase that controls the nucleation of microfractures that grow and then connect to create flow pathways. This process occurs during the primary migration of hydrocarbons in source rocks, which is the main topic of our study. It may also occur in other geological systems, such as the expulsion of water during dehydration of clay-rich sediments in sedimentary basins or serpentinite rocks in subduction zones and the transport of magmatic melts. Our system consists of a transparent, brittle gelatin material mixed with yeast and sugar. The consumption of sugar by yeast leads to CO_2 formation, resulting in microfracture nucleation and growth. We varied three parameters, (1) anisotropy (i.e., number of layers), (2) lateral sealing, and (3) rate of fluid production. We tracked fluid movement through the opening and closing of microfractures within the system. Microfracture nucleation density is similar in a layered system to previous studies (0.45 microfracture per cm^2). However, we observed that lateral confinement (0.31 microfracture per cm^2) and rate of expulsion (0.99 microfracture per cm^2) affect nucleation density and the geometrical characteristics of the microfracture network. The size, extent, and geometry of the microfracture network are dependent on all three parameters investigated, where lateral confinement and a higher rate of expulsion result in greater microfracture network connectivity. Layers control the angle of intersection between microfractures. Furthermore, layering and sealing have an impact on fracture topology. Results also show that the microfracture pattern significantly influences the fluid expulsion rate. Our results have direct applications to understanding how fluid migration occurs in low-permeability rocks through the development of a connected microfracture network produced by internal fluid generation.

1. Introduction

Natural hydraulic fracturing can form within a rock matrix due to internal fluid generation and the resulting pore pressure build-up. Initially, the internally produced fluid will diffuse through the rock matrix. However, if the rate of fluid expulsion is too high, tensile microfractures may nucleate within the rock (e.g., Anders et al., 2014; Kobchenko et al., 2014). This process occurs in the subsurface in systems that involve partial magma melt processes coupled with compaction of the solid (McKenzie, 1985; Zhu et al., 2011), the transition of hydrous to anhydrous minerals (e.g., gypsum to bassanite) (Davies, 1999; Fusseis

et al., 2012), and in the maturation and expulsion of hydrocarbons within organic-rich shale during primary migration (Tissot et al., 1974; Ozkaya, 1988; Kobchenko et al., 2011; Craddock et al., 2015).

Rock anisotropy and lateral sealing, resulting from variable porosity and permeability gradients, can exist in these geological systems. Anisotropy is prevalent in migmatites (Bons et al., 2009; Saukko et al., 2020) and is known to influence fracturing within them (Petruzalek et al., 2019). In the case of both the conversion of hydrous to anhydrous minerals and the expulsion of hydrocarbons from shales, the inherent rock structure contains two kinds of anisotropy because of i) sedimentary layering (e.g., Fusseis et al., 2012; Kobchenko et al., 2011; Anders

et al., 2014; Backeberg et al., 2017) and ii) the composite microstructure of the shale rocks that contain planar clay particles. Lateral sealing may occur due to the lateral variations of permeability and porosity of the mantle in partial melting processes (McKenzie, 1984; Takada, 1989; Zhu et al., 2011). Lithological changes and structural elements can create lateral sealing in environments where shale and gypsum are present (Demaison and Huizinga, 1991).

Layering anisotropy in organic-rich shales has been investigated utilizing wireline logs and seismic (e.g., Vernik and Liu, 1997; Sayers, 1999), image analysis (Kuila et al., 2011; Cardenes et al., 2021; Johnson et al., 2022b), and modelling – both computational (Chauve et al., 2020; Rabbel et al., 2020) and experimental (Johnson et al., 2021). Similarly, fluid generation rates have been studied using wireline logs and seismic (e.g., Li et al., 2003; Takei, 2017), image analysis (Sorbadere et al., 2018), and modelling – both computational (Hirschmann et al., 1999; Bourdon et al., 2003) and experimental (Kobchenko et al., 2014). The studies of anisotropy and fluid expulsion within organic-rich shales reviewed here occur at a number of different scales, from the regional scale (e.g., seismic) to the microscale. For organic-rich shales within the context of primary migration, the present study is best applied at a finer scale (i.e., mm-cm), wherein microfractures form and connect with one another. While lateral sealing often exists in the subsurface, it is also frequently used to control fluid expulsion in laboratory experiments. For example, lateral seals were used by Fusseis et al. (2012) for the thermal dehydration of gypsum, resulting in internal fluid generation and microfracturing. Experimental studies that induced artificial maturation of organic-rich shale have also utilized a lateral seal both in-situ and ex-situ (e.g., Craddock et al., 2015; Romero-Sarmiento et al., 2016; Panahi et al., 2019).

In geological systems, the rate of fluid migration depends on the rate of microfracture formation and growth, as well as pore fluid pressure diffusion through the medium (Bons and van Milligen, 2001; Kobchenko et al., 2014). The rate of creation of drainage pathways is critical to converting hydrous to anhydrous minerals (Fusseis et al., 2012). Variations in kerogen content and heating source can drive different rates of microfracture nucleation and growth in organic-rich shales (Kobchenko et al., 2014; Ougier-Simonin et al., 2016; Rabbel et al., 2020; Johnson et al., 2022a; Johnson et al., 2022b).

Here, we have developed a simple analogue model to explore the behavior of an elastic medium with internal fluid production, based on previous experimental setups utilizing sugar, yeast, and gelatin (Kobchenko et al., 2013; Kobchenko et al., 2014; Vega and Kovscek, 2019). Prior to these studies, gelatin has been used to model other subsurface processes, including the segregation and ascent of magma and hydrofracturing (Dahm, 2000; Bons et al., 2001; Rivalta et al., 2005). We explore three parameters that can interact with one another during reaction-induced fracturing. First, we studied the effect of structural anisotropy (i.e., rock layering). Second, we investigated the effect of lateral sealing or compartmentalization of the system. Third, we varied the rate of internal fluid production. Each parameter was tested alone against a base case where the solid contains only one layer, is not laterally sealed, and shows a fixed rate of fracturing. Then, we subsequently tested combinations of the three parameters. While each parameter has an impact on the microfracturing kinetics, they can interact with another with a positive or a negative feedback loop.

2. Methods

2.1. Experimental protocol

The experimental setup consists of a Hele-Shaw cell, 40×40 cm, with open boundaries, creating a quasi-2D environment. A 3 mm thick gelatin layer is emplaced within the cell, simulating a low permeability elastic and brittle material. CO_2 gas is internally produced utilizing a combination of sugar (sucrose) and yeast mixed together in the gelatin in order to induce fermentation (Fig. 1).

The Hele-Shaw is made up of two 10 mm thick glass plates separated by a 3 mm gap filled with the gelatin, yeast, and sugar mixture. The plates are clamped together. A white LED light source of 60×60 cm backlights the experiment. A Nikon D5300 camera records the ongoing fracturing process in the Hele-Shaw cell (Fig. 1a). A temperature sensor is located near the Hele-Shaw cell in order to track the laboratory ambient conditions (Fig. 1a). The temperature for all experiments was 16.7 ± 0.3 °C. It is critical that the gelatin stays within the temperature range of 16 ± 2.0 °C to ensure it remains mechanically brittle (Parker and Povey, 2010; Kobchenko et al., 2013; Kavanagh et al., 2018). Above this temperature range, the gelatin would behave viscously.

A volumeter is utilized to measure the production of CO_2. A volume of the same gelatin utilized for the Hele-Shaw experiment is placed into a bottle with a tube that feeds into a water-locked graduated cylinder. Production of CO_2 is then tracked with a second Nikon D5300 camera through the displacement of water by CO_2 from the graduated cylinder into the surrounding volumetric beaker (Fig. 1b). CO_2 production rate is dependent on the reaction rate of sugar and yeast. This study confirms that the use of sugar and yeast results in a consistent production rate, as established in previous studies (Kobchenko et al., 2013; Kobchenko et al., 2014; Vega and Kovscek, 2019).

Several studies have shown that, in such systems, ethanol is produced (Bai et al., 2008; Hendersen et al., 2013; Matthew et al., 2015; Beigbeder et al., 2021). However, under both the relatively low temperature of our experiments (16 °C) and low sugar concentrations used, these studies showed that very little ethanol could be produced. Therefore, we neglected the possible effect of ethanol production in our experiments.

The same Hele-Shaw cell was used for all experiments (Fig. 2). It was carefully cleaned between each experiment. This was done first by rinsing it with water and detergent, followed by distilled water, and finally ethanol. This procedure ensures good adhesion of the gelatin to
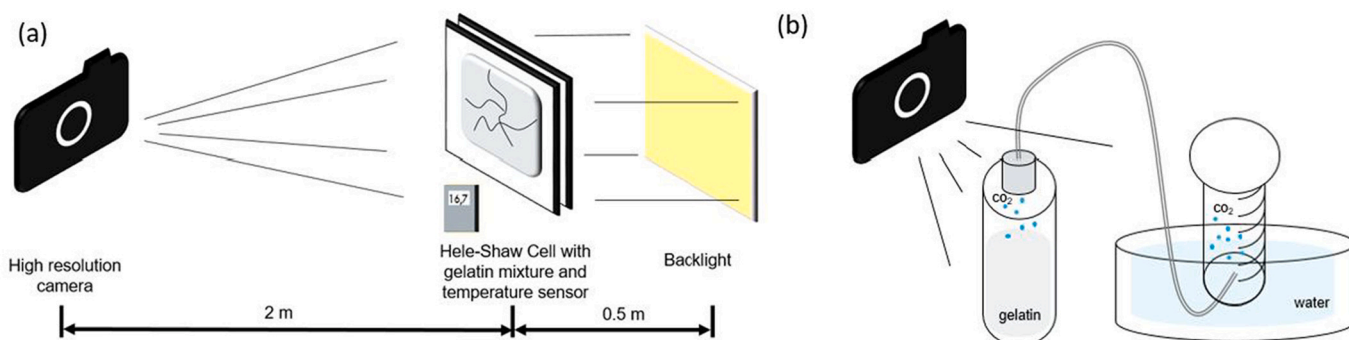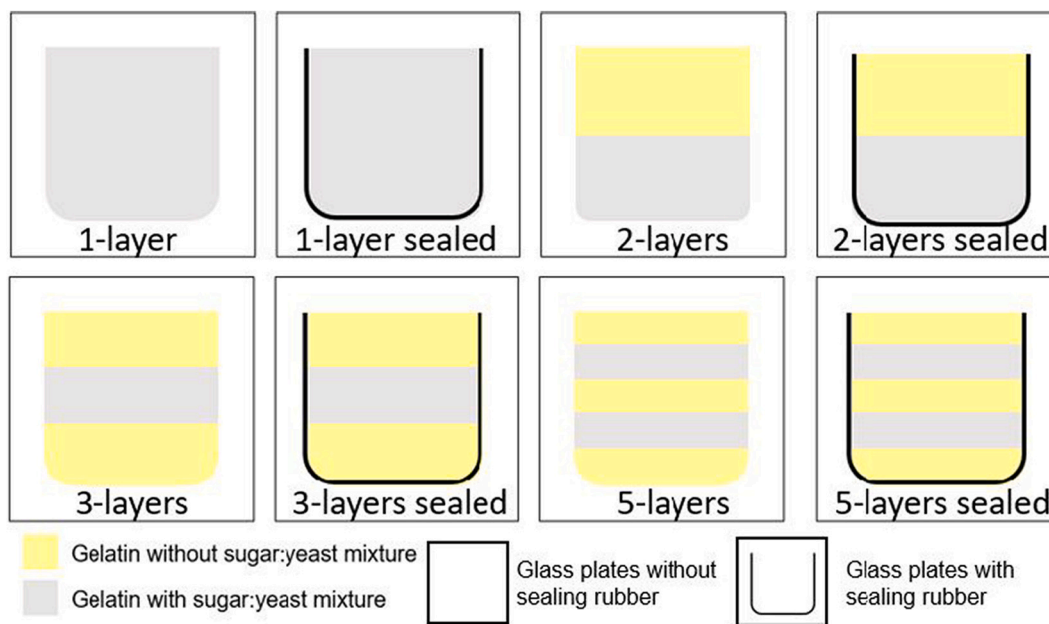

Fig. 1. The experimental setup (a) includes a high-resolution camera, Hele-Shaw Cell with gelatin matrix, temperature sensor, and backlighting. (b) A volumetric setup is used to measure the rate of CO_2 production in each experiment, with a camera used to ensure a consistent rate of gas production.

Fig. 2. Sketches of the different experiment types, including 1-layer, 2-layers, 3-layers, and 5-layers setups. Some experiments were partially sealed on three edges by a rubber o-ring, the other ones were performed under open conditions. The concentration of the sugar:yeast mixture also varied between 0.5×, 1.0×, and 1.5× for every setup variation shown here (Table 1). The Hele-shaw cell (i.e., glass plates) has dimensions of 40 × 40 cm and an opening of 3 mm between the two plates.

the glass, which prevents the accumulation of a CO_2 layer along with the interfaces between the gelatin and the glass plates. This is important as an accumulation of gas at the interfaces between the plates, and the gelatin reduces the production of microfractures in the gelatin.

To prepare the gelatin mixtures, a set number of gelatin plates (24 g of Gelita gelatin) are placed first in cold water for five minutes to soften the gelatin and then placed in 300 ml boiling distilled water to dissolve. Then, this water-gelatin mixture was left to cool down to 25 °C before the mixture of sugar and yeast was added. If the yeast is added to the water at a temperature higher than 25 °C, it may die. For the reference case, we added 3 g of sugar and 1 g of yeast per liter of water, which corresponds to the reference case 1.0× in Table 1. We also used 0.5× and 1.5× concentrations of yeast and sugar. Then, a rubber strip was placed along three edges between the glass plates for sealing purposes before the liquid was poured into the Hele-Shaw cell. We then placed the cell vertically into a refrigerator set to 4 °C such that the gelatin could

solidify while the yeast remained effectively dormant. After one hour of curing, the cell was rotated 90° and placed horizontally in the fridge in order to ensure good adhesion between the gelatin and the glass plates. The total curing time was 24 h. Once cured, the sealing rubber was either removed for experiments not laterally sealed or left in place for experiments that were partially sealed (Fig. 2).

In total, 21 experiments were performed under varying three parameters: 1) the number of layers within the Hele-Shaw cell, 2) the concentration of sugar and yeast inside certain gelatin layers, and 3) whether or not the experiment is sealed on three edges (Table 1). For some conditions, several experiments are performed to verify the reproducibility of the results. Sixteen experiments were quantitatively analyzed for 2D microfracture patterns and fluid migration, and the remaining five experiments were qualitatively analyzed. For one of these five experiments, the CO_2 diffused outside of the cell, and no microfracture formed because of the too low concentration of sugar and yeast (0.5×). The remaining four experiments contained a microfracture pattern; however, overpressure resulted in a loss of adhesion between the gelatin and the glass plates of the Hele-Shaw cell and an accumulation of gas along with the interfaces.

The first parameter varied is the number of gelatin layers. Experiments were tested with one layer, two layers, three layers, and five layers (Fig. 2 and Table 1). For the 2-layers, 3-layers, and 5-layers experiments, layers that contain a mixture of sugar and yeast alternate with layers that do not. Efforts were made to ensure proper welding between the layers, including introducing the newest layer at a temperature several degrees warmer than the layer already emplaced (Kavanagh et al., 2017). Very slight differences in elastic properties have possibly been introduced due to variable composition between the layers (Brizzi et al., 2016; Sili et al., 2019), and we neglected this effect. For the 2-layers experiment, the bottom layer contains a mixture of sugar and yeast. The 3-layers experiment contains a mixture of sugar and yeast in the middle layer. The 5-layers experiment contains sugar and yeast mixture in layers 2 and 4 (Fig. 2). In addition to varying the number of layers, two other parameters were varied for some of the experimental setups. Experiments were either partially sealed, with a rubber o-ring, on three edges or not. Finally, the ratio of sugar and yeast was varied in the range of 0.5×, 1.0×, and 1.5× the standard mixture of

Table 1
List of experiments, number of experiments performed, and parameters.

Experiment	Ref. case (1.0× yeast + sugar)	Sealed (rubber)	Low ratio (0.5× yeast + sugar)	High ratio (1.5× yeast + sugar)	High ratio, sealed (1.5× yeast + sugar)	Total
1-layer	1	1	0	1	1*	3 + 1*
2-layers	1	1	0	1	1*	3 + 1*
3-layers	3	1	1	1	1*	6 + 1*
5-layers	3	1	0	1*	1*	4 + 2*
Sum	8	4	1	3 + 1*	4*	16 + 5*

Note – The five experiments marked with '*' experienced overpressure resulting in gas accumulation at the interface between the gelatin layer and the glass plates. This bias made it impossible to perform quantitative image analysis. Therefore, these experiments are used for discussion purposes only. The remaining sixteen experiments were used for quantitative image analysis.

sugar and yeast per setup (Table 1).

The dimensions of the layers (thickness of 3 mm and height) were the same between experiments with the same number of layers by prescribing a defined amount of gelatin for every layer. The height of all layers was then measured afterward to ensure consistency. In the 5-layers 1.5× sugar:yeast mixture experiment, fluid overpressure occurred, leading to a detachment between the glass and the gelatin in the Hele-Shaw cell. The sealing of three of the four edges of the Hele-Shaw cell was done utilizing the same rubber strip used during the gelatin curing process.

2.2. Image analysis and microfracture characterization

A Nikon D5300 camera was used to collect 16-bits RGB images of the Hele-Shaw cell every 15 s for a minimum of 36 h. Every experiment produced a set of time-lapse images that displayed the nucleation and growth of microfractures with time as the result of the production of CO_2 gas from the reaction between the yeast and sugar. Images were first preprocessed, including image cropping, masking, artifact removal, and thresholding. We then quantitatively analyzed the microfracture networks.

The following workflow was used for the preprocessing of all images. First, all images were reviewed to provide a visual reference for cropping and converting the RGB images into a single-channel grayscale image. We corrected the images from backlight intensity variations and any other subtle changes in light settings. The baseline light settings are set to the initial image at time $t = 0$. Each subsequent image is normalized to this initial image so that only the development of microfracture nucleation sites and the resulting microfracture network is captured. A mask is created using the final image, with the complete microfracture network, in order to isolate the salient information from the rest of the image. Gray scale thresholding is applied to extract the microfractures and microfracture network through time for the entirety of each experiment. The connectivity of the microfractures was analyzed by labeling with a different color every connected set of microfractures and by identifying each microfracture extremity.

Our data contain the microfracture nucleation sites and the subsequent growth and interactions of microfractures with each other. Microfracture interactions with the interfaces between layers with

different gelatin mixtures are also followed. Upon the initial development of microfractures, every nucleation site is assigned an ID# that follows every new microfracture. Microfracture nodes are defined as any location(s) where microfractures that have a unique nucleation point meet (Fig. 3). Angles δ (Fig. 3a) when microfractures coalesce are measured for all microfracture nodes. In addition, the microfracture network is described by the parameter ω, defined as:

$$\omega = \frac{n_d - n_j}{n_d + n_j} \tag{1}$$

where n_d is the number of microfractures terminated by dead ends, n_j is the total number of microfracture junctions (Fig. 3a). The parameter ω quantifies the microfracture network in terms of two endmembers. If the network is fully connected and contains only microfractures that are connected to other microfractures or to the system boundaries ($n_j = n_d$), then $\omega = 0$. If the network contains isolated microfractures ($n_j = 0$), then $\omega = 1$. A fracture network branching event occurs when none or one of the two growing microfracture tips connects with another given microfracture. A fracture network fragmenting event occurs when both of the growing microfracture tips interact with other given microfractures or the system boundaries.

A microfracture-layer node is defined as a location where a microfracture tip interacts with the interface between two gelatin layers. The angle of deflection, θ (Fig. 3b), is also measured for all microfracture-layer nodes.

Utilizing ω, calculated from dead-end and junction nodes (Fig. 3a), the influence of structural changes to the system (i.e., introducing anisotropy) can be understood. In addition to this, the XYI classification of microfracture nodes can be utilized to characterize the rate of fluid flow a system can maintain (Sanderson and Nixon, 2015; Alvarez et al., 2021; Silva et al., 2021). With the framework of XYI-nodes (Fig. 3c), the number of branches, N_B, can be calculated:

$$N_B = \frac{1}{2}(N_I + 3N_Y + 4N_X) \tag{2}$$

from the number of I-nodes (NI), Y-nodes (NY), and X-nodes (NX) within a microfracture network from a given gelatin experiment. It has been hypothesized and later empirically shown that I-nodes are the least permeable (i.e., poorly connected) pathways and that Y-nodes are the
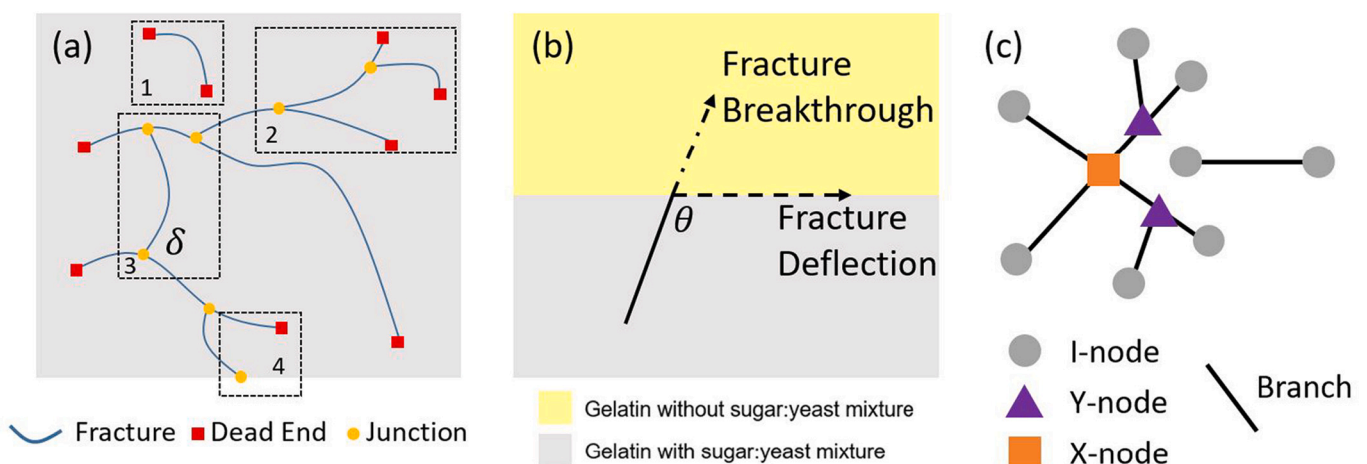
Fig. 3. (a) Four scenarios have been highlighted to show how individual microfracture nodes are characterized by the number of dead ends (red squares), n_d, and the number of junctions (orange circles), n_j, results in a more fragmented or branching network. (1) A microfracture that does not interact with another microfracture at both ends represents an isolated branch in the fracture network. (2) A dendritic (i.e., river-like) pattern will result in a greater number of dead-ends points than junctions. (3) Cross-cutting microfractures will result in a fragmentation event in the network. The angle between two microfractures is δ. (4) A node at the matrix boundary is considered as a junction, while a node within the boundary is considered as a dead-end. (b) Microfracture propagation will either deflect at the layer interface with an angle θ or will continue to propagate into the layer above (i.e., breakthrough event). (c) An alternative method of identifying nodes depends on the relationship that node has with the branches it's connected to. A node connected to one branch is an I-node, with three branches is a Y-node, and with four branches is an X-node. (For interpretation of the references to color in this figure legend, the reader is referred to the web version of this article.)

most permeable (i.e., well connected) pathways (Sanderson and Nixon, 2015; Silva et al., 2021). The parameter ε, calculated from the ratio of nodes, can be used as a proxy to quantify the ability of a fluid to flow through a given fracture network:

$$\varepsilon = \frac{N_I + 3N_Y + 4N_X}{N_I + N_Y} \tag{3}$$

The opening and closing of fractures can also be used to track fluid flow within the experiments. The procedure of image analysis applied to the entire image sequence captures the total surface area of the aperture of open microfractures at a given moment in time, A(t). The Fourier transform of the time series A(t) is used to capture the dynamics of fluid movement within the Hele-Shaw cell. The low-frequency trend is subtracted from the time series, and the discrete Fourier transform ($|Y(f)|$) is calculated. The power spectrum (($|Y(f)|)^2$) of the Fourier transform for each experiment shows a well-pronounced peak that indicates the dominant frequency of closing-opening dynamics of the microfractures and fluid expulsion process.

3. Background theory

3.1. Principles of linear elastic microfracture mechanics

Fluid-driven tensile microfracture propagation within organic-rich shales, similar to magmatic intrusion during dyke propagation, can be described, to a first order, using linear elastic microfracture mechanics (Lister and Kerr, 1991; Clemens and Mawer, 1992; Rivalta et al., 2015). In both situations, a fluid moves throughout a brittle solid matrix, driven by fluid pressure gradients (Nur and Byerlee, 1971; Secor and Pollard, 1975; Bear, 1975). Once a critical fluid pressure gradient threshold is reached, the release of pressure is achieved (Coulomb, 1776) through the formation of tensile microfractures in the solid (e.g., Anders et al., 2014). The balance of pressure necessary for a tensile microfracture to propagate under the effect of an internal increase of fluid pressure is described in the literature (e.g., Griffith, 1921; Secor, 1965; Lister and Kerr, 1991; Clemens and Mawer, 1992; Kavanagh et al., 2006; Kobchenko et al., 2014; Vega and Kovscek, 2019). For a microfracture to propagate, the fluid pressure in the microfracture, P_p, must be larger than the fluid pressure, P_e, that maintains a microfracture open and in equilibrium.

$$P_e = \frac{E}{2(1 - v^2)} * \frac{w}{y} \tag{4}$$

where E and v are Young's modulus and Poisson's ratio of the gelatin, w is half the aperture of the microfracture, and y is half the second smallest dimension of the microfracture. Microfracture propagation occurs when the dissipation of strain at the tip of the microfracture overcomes the microfracture toughness, K_c:

$$K_c = \sqrt{2\gamma_s * E} \tag{5}$$

where γ_s is the surface energy necessary to break the gelatin. The fluid pressure at the onset of microfracture propagation, P_p, is then expressed:

$$P_p = \frac{K_c}{\sqrt{\pi * l}} \tag{6}$$

where l is the length of the crack. For a system in equilibrium, $P_p \leq P_e$, whereas a microfracture propagates when $P_p > P_e$. The Poisson's ratio for gelatin is close to 0.5 (Kavanagh et al., 2013; Van Otterloo and Cruden, 2016; Vega and Kovscek, 2019). The values of Young's modulus (E) are reported in the range ~ $1.5 \cdot 10^5$–$8.35 \cdot 10^5$ Pa (Kavanagh et al., 2013; Van Otterloo and Cruden, 2016; Vega and Kovscek, 2019). Kavanagh et al. (2013) and Vega and Kovscek (2019) report surface energy for gelatin equal to 1 J m^{-2}. We used these values to calculate the parameters in eqs. 4–6.

3.2. Microfracture formation and fluid migration

The consumption of sugar by the yeast produces CO_2, which subsequently diffuses through the gelatin matrix (Kobchenko et al., 2013; Kobchenko et al., 2014). In order for a microfracture to nucleate, a critical supersaturation is needed. This is calculated as follows:

$$p_c = \frac{c_c}{k_H} \tag{7}$$

where c_c is the concentration of the dissolved CO_2 required for the nucleation of a gas bubble, p_c is the pressure required to nucleate a microfracture using the ideal gas approximation, and k_H (mL·atm/mol) is Henry's coefficient that relates the diffusion kinetics to the partial pressure of the gas. Kobchenko et al. (2013) determined that diffusion of the CO_2 from the gelatin matrix to the fractures controls the growth of microfractures, which is described by:

$$\delta_c = \sqrt{\frac{2D}{\gamma} \frac{p_c - p}{k_H}} \propto \gamma^{-\frac{1}{2}} \tag{8}$$

where, δ_c (m) describes the critical distance between microfractures, γ is the gas production rate (mL/h), D is the diffusion coefficient of CO_2 in the gelatin and is equal to $1.85 \cdot 10^{-9}$ m^2 s^{-1}, and p is the gas pressure determined from the concentration of the dissolved CO_2 (atm).

Once a microfracture has nucleated, the rate of microfracture growth follows:

$$l = l_0 exp\left(\frac{2\varphi RTt}{p_c a}\right) \tag{9}$$

where l is the microfracture length, l_0 is an integration constant that characterizes the critical length above which a gas bubble evolves into a microfracture, φ is the flux of CO_2 (mol·m^{-2}·h^{-1}), R is the ideal gas constant, T is temperature, t is time, and a is microfracture aperture. Microfracture aperture is limited to $a = 3$ mm due to the adhesion of the gel to the walls of the Hele-Shaw cell (Kobchenko et al., 2013).

When a microfracture reaches an open outside edge of the Hele-Shaw cell, the CO_2 flows out of the experimental setup. Gas expulsion out of the system is controlled by the intermittent opening and closing of microfractures. The drainage network is influenced by the microfracture topology and connectivity.

4. Results

Gas production as the reaction between sugar and yeast was measured by the CO_2 production tracker (Fig. 1). The start times for CO_2 production range from 10 min to three hours after the experiment has begun (Fig. 4a). In this stage, the diffusion of gas is impossible to vizualize in the Hele Shaw cell but can be detected by the CO_2 production tracker. The timing of the initial microfracture nucleation depended on the concentration of the sugar:yeast mixture, with experiments that had 1.5× sugar:yeast ranged in start times from ~5:45–7:15 h. Experiments with the normal (1.0×) concentration started in the range ~ 12:30–17:30 h (Fig. 4b).

During the initial stages of microfracture propagation, the microfractures nucleate in a penny-shape and then may propagate from one or both ends until they reach the edge or coalesce with another microfracture (Fig. 4c). Microfracture creation continued for ~35 h until the final microfracture pattern is obtained (Fig. 4d). The number of layers or the presence of sealing appears to have no apparent impact on the amount of time to CO_2 production, initial microfracture nucleation, and total experiment duration. However, layers introduce the possibility for microfractures to either penetrate or be deflected by the interface (Fig. 4d). Further to this, sealing three edges fundamentally changes the way microfractures interact with one another, as discussed below.
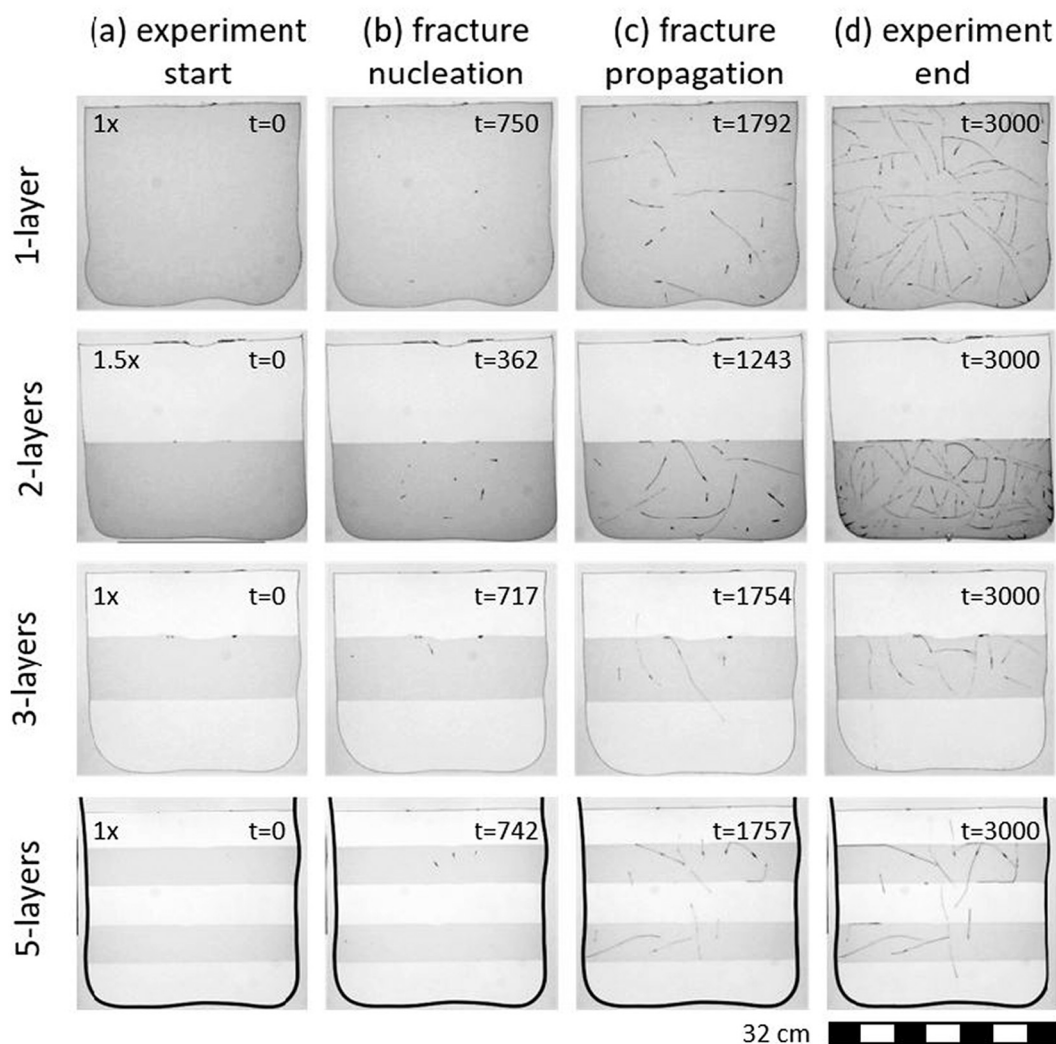
Fig. 4. Time series showing the evolution from (a) start of the experiment, (b) initial microfracture nucleation, (c) microfracture development and interaction, and (d) final microfracture network pattern for 1-layer sugar:yeast concentration 1.0×, 2-layers sugar:yeast concentration 1.5×, 3-layers sugar:yeast concentration 1.0×, and 5-layer sealed and sugar:yeast concentration 1.0× experiments. These raw images are processed to extract the microfractures over time. Time is given in minutes. Gelatin layers with a darker gray shade contain the sugar:yeast mixture.

4.1. Microfracture nucleation and growth

The nucleation site of every microfracture is identified in both space and time for all experiments (Fig. 5). Every nucleation site is given an identification number (ID#) so that the continued growth of the microfracture network is tracked.

The distribution of nucleation sites appears to be dependent, or at least influenced by all parameters that were varied: the number of layers, the composition of the mixture of sugar and yeast, and whether or not the gelatin is sealed on three edges. This influence is more pronounced with some variables than it is for others (e.g., the introduction of layers without sugar and yeast prevents nucleation in certain areas). For the simplest case (i.e., one layer, open, 1.0× sugar:yeast), there is a spatially random distribution of 53 nucleation sites, with a density of 0.58/cm² (Fig. 5, left column). The density of nucleation sites, when normalized by the surface area of the gelatin layers that contain the mixture of yeast and sugar, is 0.48/cm² (28 nucleation sites), 0.40/cm² (12 nucleation sites), and 0.44/cm² (14 nucleation sites) for two layers, three layers, and five layers respectively (Fig. 5). Therefore, the density of the nucleation site is comparable when varying the number of layers. However, the nucleation sites form across a greater range of time for layered experiments (Figs. 5, S1).

An increase in sugar and yeast concentrations results in a greater density of nucleation sites (Fig. 5). The average nucleation density for 1.5× sugar:yeast experiments is 0.99 ± 0.20/cm². This value corresponds to an increase of 0.44/cm², ~2× increase in density due to a 1.5× increase in sugar:yeast concentration. Nucleation site density for 1-layer, 2-layers and 3-layers experiments are 1.27/cm² (118 nucleation sites), 0.91/cm² (49 nucleation sites), and 0.80/cm² (25 nucleation sites). Values for 5-layers experiments are not available due to the overpressure in the Hele-Shaw cell. A larger number of nucleation sites through time is observed for the 1.5× sugar:yeast concentration experiments (Figs. 5, Fig. S1).

Sealing on three sides, utilizing a rubber o-ring, also causes a change in the number of nucleation sites (Fig. 5). The average nucleation density for the partially sealed experiments is 0.31 ± 0.13/cm², representing a decrease of ~36% compared to open experiments. Nucleation site density for 1-layer, 2-layers, 3-layers, and 5-layers experiments are 0.31/cm² (28 nucleation sites), 0.14/cm² (8 nucleation sites), 0.50/cm² (16 nucleation sites), and 0.30/cm² (12 nucleation sites). Like open experiments, an increase in the number of layers results in nucleation sites having a greater distribution through time (Fig. 5, S1).

Microfracture growth over time occurs with similar kinetics for all experiments. After an initial period of quiescence due to diffusion of CO_2
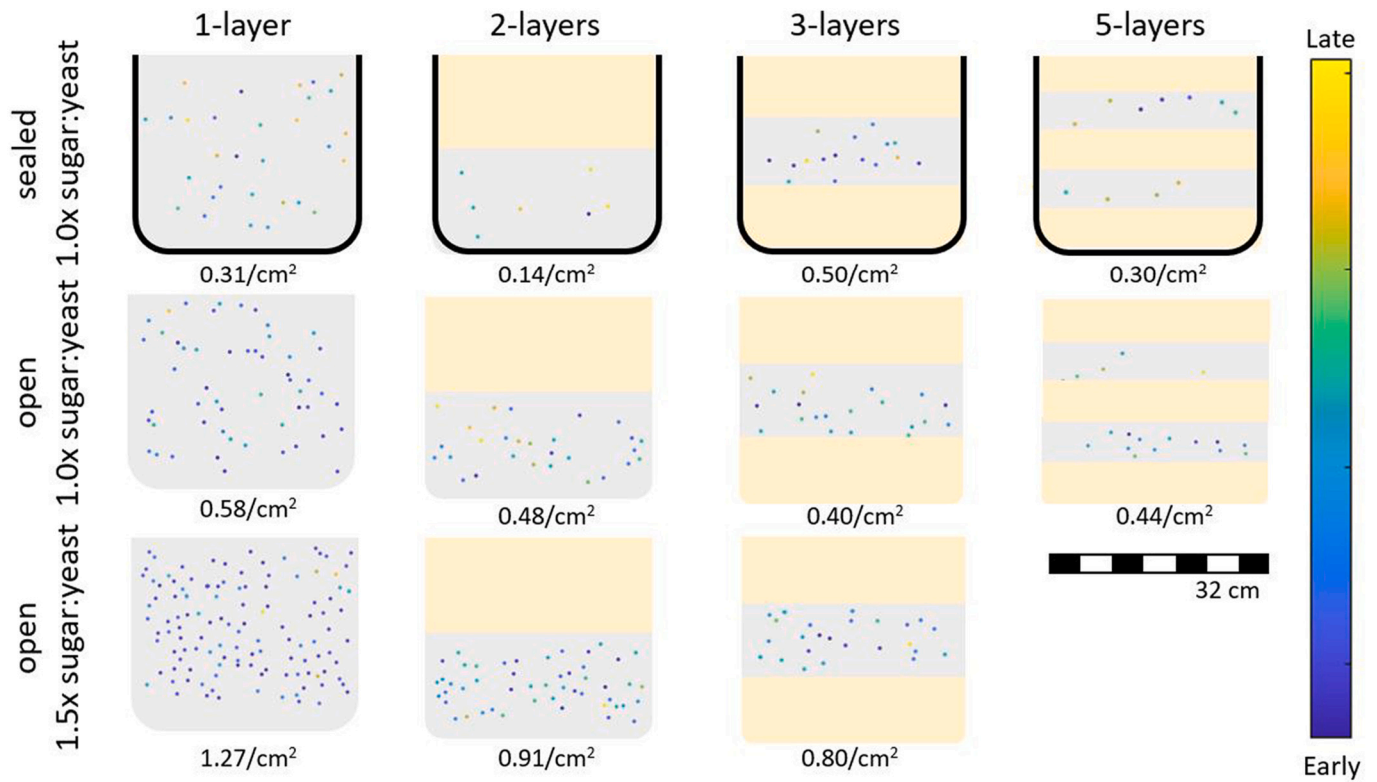
Fig. 5. Microfracture nucleation points and density for all experimental types. The color scale indicates the time.

throughout the matrix (Phase I, Fig. 6), a period of microfracture rapid growth occurs as microfractures first nucleate and then propagate (Phase II, Fig. 6). The transition point between Phase I and II is based on reaching a threshold at ~20% of the total fracture length calculated from an average of all the experiments. There is an acceptable standard deviation across all experiments of $+/-$ 4%, with slight variations

Fig. 6. Cumulative microfracture length shows a sigmoidal evolution with time for all experiments. Black vertical lines separate approximately the three phases of fracture network growth discussed in the text.

among the different experiment types. A greater number of initial nucleation points (e.g., 1.5× sugar:yeast experiments) results in a slightly higher threshold.

Conversely, a lower number of initial nucleation points (e.g., 1.0× sugar:yeast sealed experiments) results in a slightly lower threshold (Fig. 6). Finally, microfracture growth plateaus as a fully developed microfracture network are able to drain the gas produced, and the sugar becomes totally consumed by the yeast (Phase III, Fig. 6). Comparisons between experiments with the same number of layers reveal how experiment type influences the cumulative microfracture length. Experiments with a higher sugar:yeast concentration have the highest cumulative microfracture length. Experiments with the 1.0× sugar:yeast concentration have the next most microfracture length, and sealed experiments have the least (Fig. 6). The total microfracture length for the 1.5× concentration of sugar and yeast is ~500 cm, while it is ~300 cm for the 1.0× concentration of sugar and yeast. Sealed experiments had a smaller total microfracture length up to ~250 cm, indicating that alterations in the concentration of sugar and yeast had a larger impact on the total microfracture network length, whether the experiment was open or partially sealed (Fig. 6).
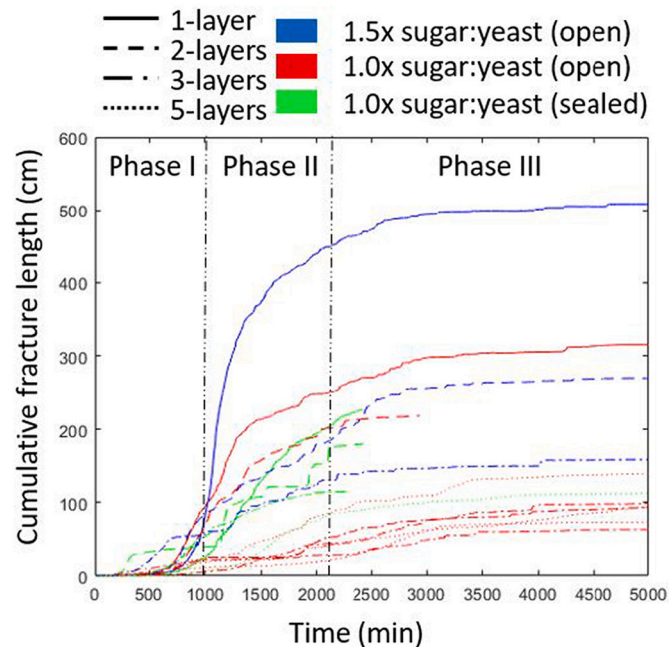
Microfracture growth over time is characterized by a sigmoidal growth curve for all experiments. However, 1-layer experiments show a nearly perfect sigmoidal shape (Fig. 6). For the 2-layers and 3-layers experiments, this shape is disrupted whenever slower microfracture growth occurs as a result of microfractures penetrating the non-active gelatin layers (Figs. 4 and 6). Microfracture growth accelerates again whenever microfractures connect. This intermittent growth pattern is perhaps most visible in the sealed experiments (Fig. 6), which also had the greatest distribution of microfracture nucleation sites over time (Fig. 5). This typical sigmoidal growth shape is further influenced in 5-layers experiments, wherein fracture nucleation does not always begin simultaneously in the two different active layers (Figs. 4 and 6).

The 3-layers and 5-layers experiments contain a nearly identical amount of active and inactive gelatin and are therefore ideal to compare

the effect of layering on the total microfracture length. For the 3-layers and 5-layers open experiments, which were all reproduced several times (Table 1), values range from ~50–130 cm for total fracture length, and the variation is due to experimental variability.

The connectivity of microfracture patterns is labeled with colors in Fig. 7, where each color represents a fully connected set of microfractures. Microfracture density is greatest for the 1.5× concentration of sugar and yeast and lowest for sealed experiments (Fig. 7), which is in line with higher nucleation site densities (Fig. 5). Likewise, microfracture density generally decreases with an increasing number of layers; however, there is some similarity between 3-layers and 5-layers experiments (Fig. 7). Connectivity of the microfracture network is higher for both the sealed and high sugar:yeast concentration experiments than for the open 1.0× sugar:yeast concentration experiments (Fig. 7). Connectivity in the microfracture network is the result of two different processes. In the case of the high sugar:yeast concentration experiments, higher nucleation density results in a greater number of microfractures, that become ultimately better connected. In the case of partial sealing utilizing a rubber o-ring on three sides, connectivity is required for the created CO_2 to exit the apparatus, despite fewer nucleation sites.

4.2. Microfracture-microfracture interactions

Microfracture growth results in individual microfractures interacting with each other, as shown by the final microfracture pattern (Fig. 7). Angles of coalescence between two microfractures, δ (Fig. 3), are measured (Fig. 8).

These angles are usually in the range of 55–90° (Fig. 8, Table S1). While the dominant coalescence angle does not change significantly until 5-layers experiments, we measured an increase in the proportion of coalescence angles between 0-54° as the number of layers increases (Table S1). Average coalescence angles based on the experiments from the present study and image analysis on experiments from Kobchenko et al. (2014) reveals one trend. The increase in sugar:yeast concentration impacts the distribution of coalescence angles. The starting point for coalescence angle is ~10° higher for 1.5× sugar:yeast concentration compared to 1.0× concentration. However, the decrease of coalescence angle with the number of layers is similar regardless of sugar:yeast concentration (Fig. 9b). There is also a general decrease in the starting angle; however, the current error for each angle (Fig. 8) is too large

compared to the decrease in starting angle to show a robust trend.

There is no apparent relationship between the concentration of the sugar:yeast mixture and ω. Note, 1.5× sugar-yeast mixture experiments show a higher than average value of ω in the 1-layer and 2-layers experiments and a lower than average value of ω in the 3-layers experiments. There is also no apparent relationship due to partial sealing, although these experiments consistently show a value of ω close to the mean value of all experiments.

The 1-layer experiments have the highest average value of ω (Eq. 1) and, therefore, the most fragmented networks, with a value $\omega = 0.38 \pm 0.07$ (Fig. 9). For 2-layers and 3-layers experiments, the average values are $\omega = 0.25 \pm 0.05$ and $\omega = 0.23 \pm 0.09$, respectively (Fig. 9). In the 5-layers experiments, the value of $\omega = 0.08 \pm 0.05$ is the lowest, corresponding to the networks with more branches (Fig. 9). A linear relationship between the number of layers and the parameter ω can be defined as:

$$\omega = -0.07l + 0.43 \tag{10}$$

wherein ω correlates negatively with an increase in the number of layers (l). Therefore, increasing the number of layers results in a shift from a fragmented microfracture network to an almost entirely branched microfracture network.

4.3. Microfracture-layer interface interactions

Microfractures interact not only with one another but also with the interface between layers that contain the mixture of sugar and yeast (i. e., active layers), and layers that do not contain the mixture (i.e., inactive layers). Certain microfractures within multi-layer experiments propagate until interacting with the active and non-active layers interfaces. When a microfracture reaches an interface, it will either breakthrough into the non-active layer or it will be deflected by the interface to propagate along with it. The angle of intersection between the microfracture and interface layer plays a critical role in whether a microfracture penetrates into the next layer or is deflected along with the interface (Figs. 3, 10). Microfracture propagation behavior changes for angles $\theta > 50°$, with significantly more deflection below this value and more breakthrough above it. The average percentage of microfractures that breakthrough for angles above 50° is 70%, and below 50°, it is 15% (Fig. 10).

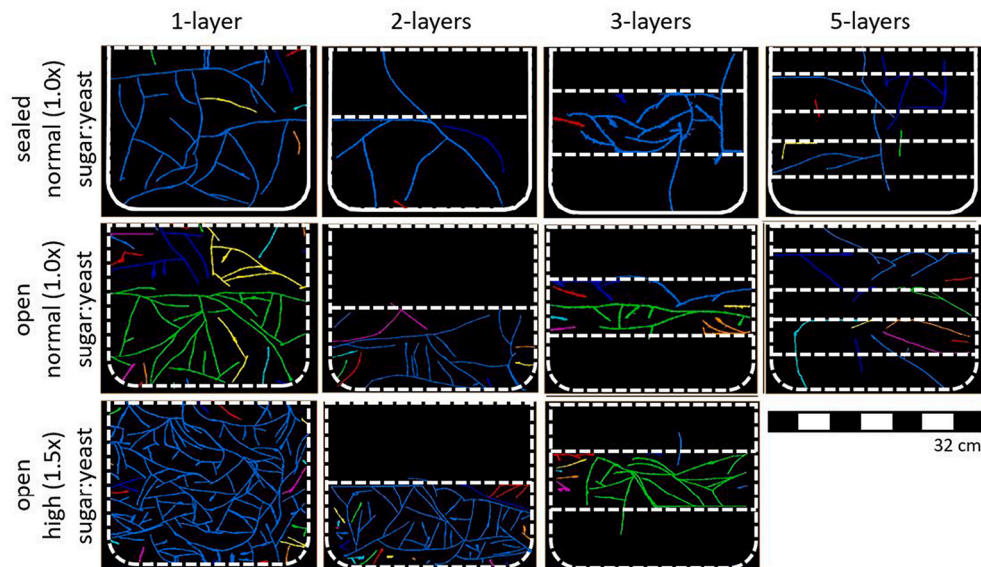The number of microfracture-layer interface interactions increases as

Fig. 7. Final microfracture patterns for representative experiments. Each color is indicative of a connected network of microfractures. Dashed white lines underline the edges and the boundary between layers. A solid white line underlines the sealed portion of some experiments.
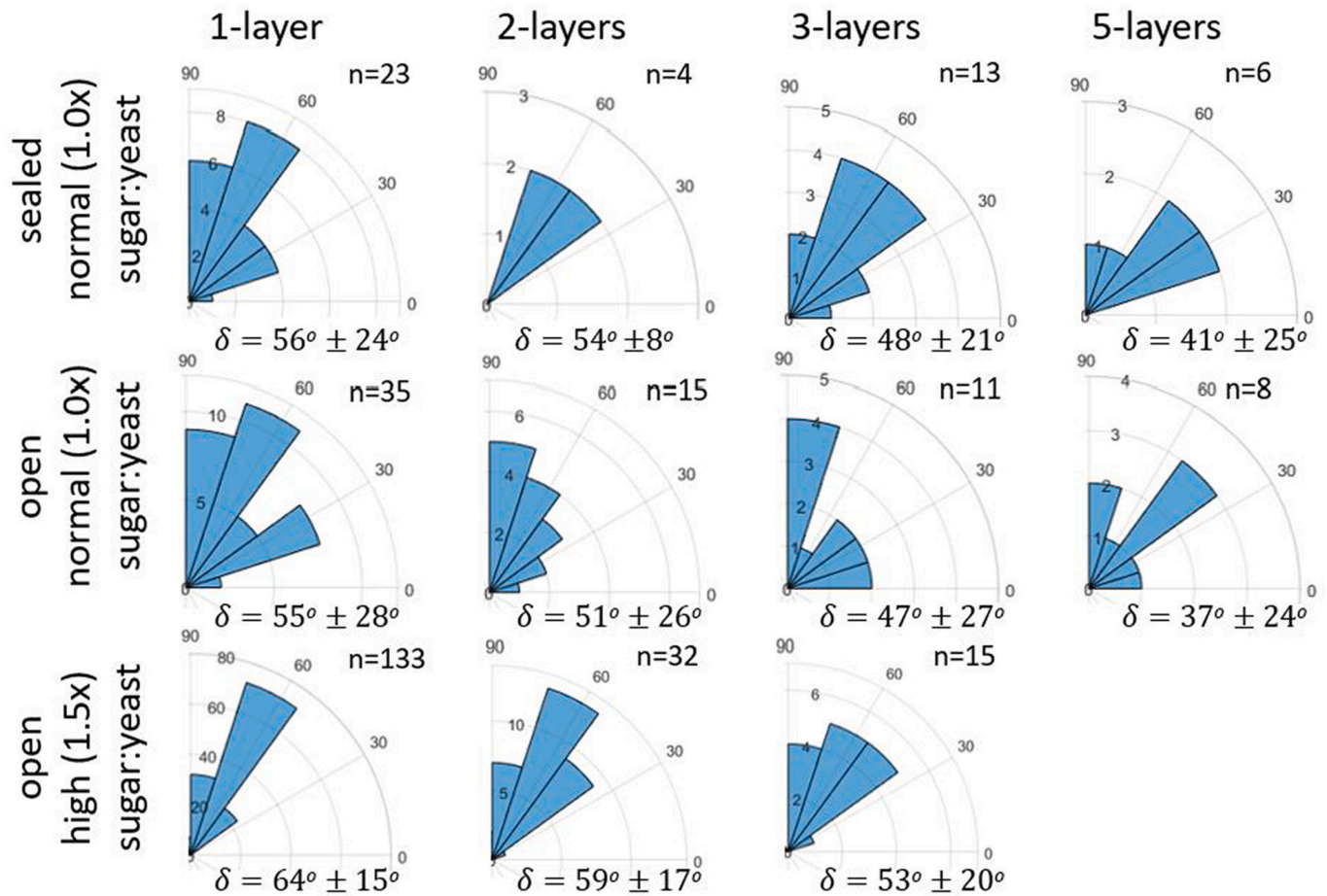
Fig. 8. Distributions of coalescence angle δ (Fig. 3) between any two microfractures for every experiment type. The mean angle and standard deviation are indicated on each plot.
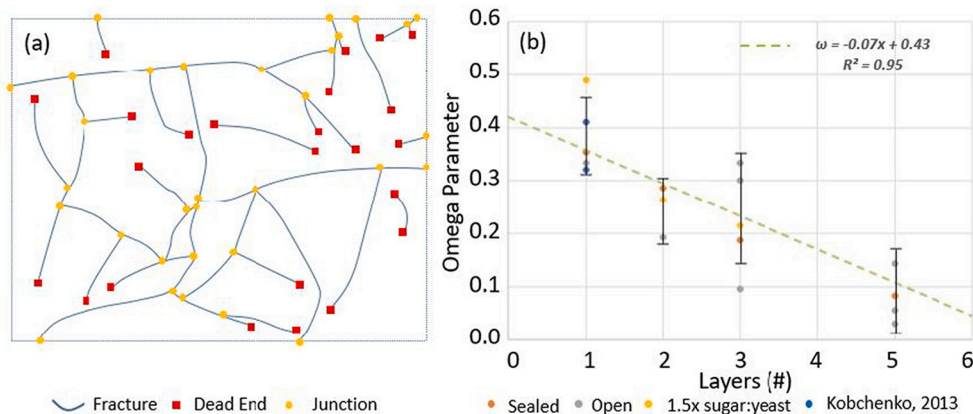

Fig. 9. a) Identification of dead-end nodes and junction nodes in the 1.0× sugar:yeast concentration 1-layer experiment. b) Relationship between the parameter ω (Eq. 1) and the number of layers.

the number of layers increases. Therefore, more data is available for experiments with more layers. Additionally, the increase in the sugar: yeast concentration from 1.0× to 1.5× implies a greater number of microfractures resulting in a greater number of microfracture-interface interactions. However, the data available indicates that the concentration of the sugar:yeast mixture has no effect on the direction of microfracture propagation. Sealing, utilizing a rubber o-ring on three sides, has a clear effect on the angle of interaction between microfractures and layers. The impact of sealing is most noticeable in the 5-layers

experiments, where the dominant microfracture angles to the interface are in the range of 70 – 90° (Fig. 10). From the data available in open experiments, increasing the number of layers results in a greater number of interactions that are more oblique (i.e., <50°) to the interface (Figs. 8 and 10).

4.4. Microfracture network connectivity and fluid flow

Once the microfracture network as a whole, or an individual
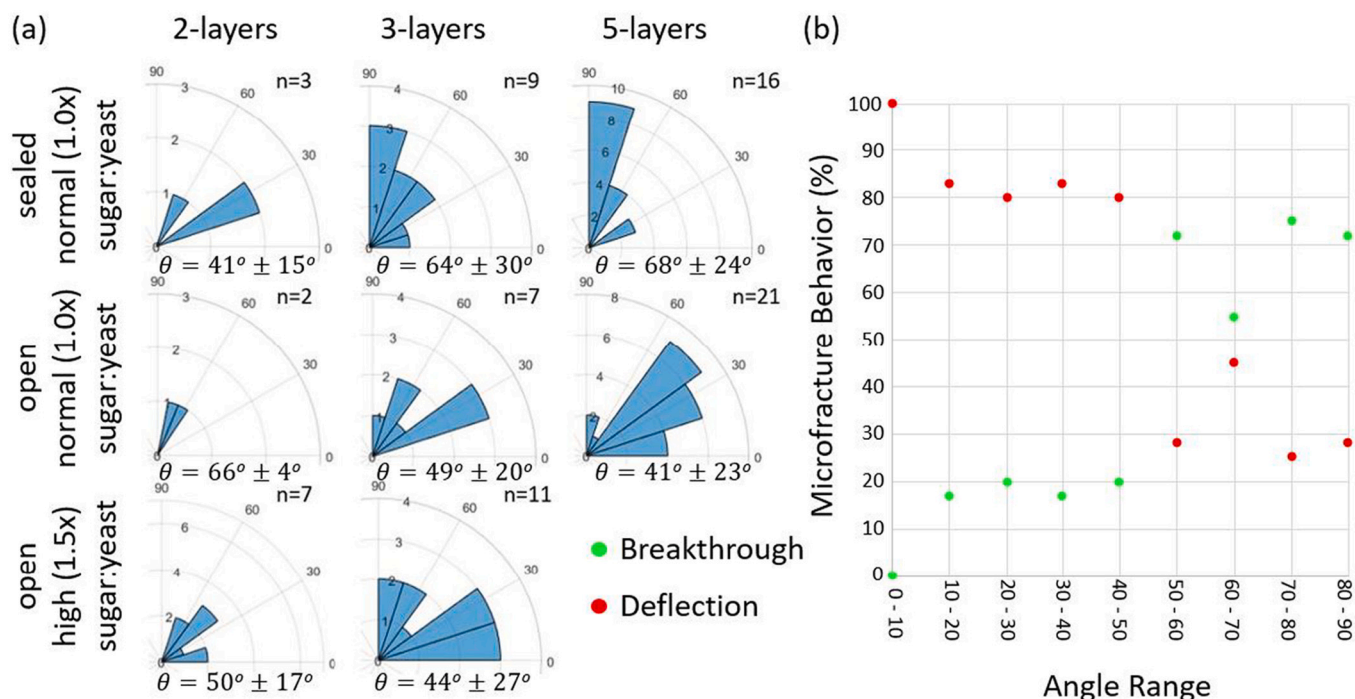
Fig. 10. Angles θ between microfractures and gelatin layer interfaces: $0°$ is parallel to the interface, while $90°$ is perpendicular. (a) The angle of intersection between a microfracture and the layer interface for all multi-layer experiments. Mean angle for each experiment, θ, is given with the standard deviation. (b) Microfracture behavior is described as either breakthrough or deflection along with the interface depending on the angle θ between the microfracture and the layer interface (see also Fig. 3b).

microfracture, is connected to an outside edge, a pathway allows the migration of the CO_2 to either other microfractures or outside of the apparatus. At this point, the fluid filling microfractures can be expelled from the gelatin resulting in the closing of microfractures. As CO_2 continues to flow from the host matrix into the microfractures, they will reopen again intermittently. This behavior can be seen when plotting the total surface area of the open microfractures as a function of time, A(t), for all fifteen quantifiable experiments (Fig. 11). An initial period of microfracture nucleation and growth correlates with Phases I and II, defined in Fig. 6. After some time, the total microfracture length plateaus and the increase and decrease in microfracture aperture surface area relate to the opening and closing of the microfracture network, corresponding to Phase III (Fig. 11). The amplitude of variation for the microfracture area is the largest in sealed experiments and smallest for open experiments with a $1.0\times$ sugar:yeast concentration (Fig. 11).

Partially sealed experiments that utilized a rubber o-ring on three sides show a greater amount of build-up time compared to other experiment types before fluid expulsion from the microfracture network occurs (Fig. 11). The greater time required for expulsion may be an indicator that the partial seal altered the ability of the system to transfer stress within its stress field (i.e., greater fluid pressure is required locally to expel fluids). This interpretation is supported by the lower nucleation density in partially sealed experiments compared to open experiments.
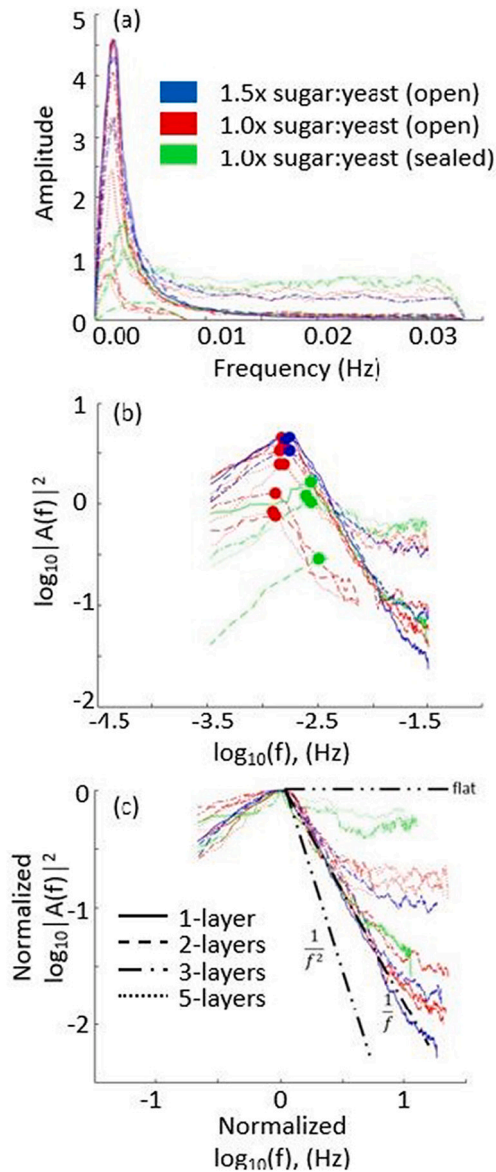
A Fourier transform was applied to the signal, A(t), in order to characterize its intermittency (Fig. 12a). The signal contains both a periodic component, identified by the main peak of the signal and a decay towards higher frequencies (Fig. 12a).

The data are plotted on a logarithmic scale (Fig. 12b) in order to compare the peak frequencies for all of the experiments. The amplitude of the peak generally correlates to the number of layers, with 1-layer experiments having the largest amplitude and 5-layers the smallest one (Fig. 12b). All experiments had a tight grouping of peak values within their experiment class. Peak frequencies for open experiments with $1.0\times$ concentration of sugar:yeast varied in the range of $10^{-2.91}$ to $10^{-2.85}$ Hz, corresponding to time scales in the range of 700–800 s
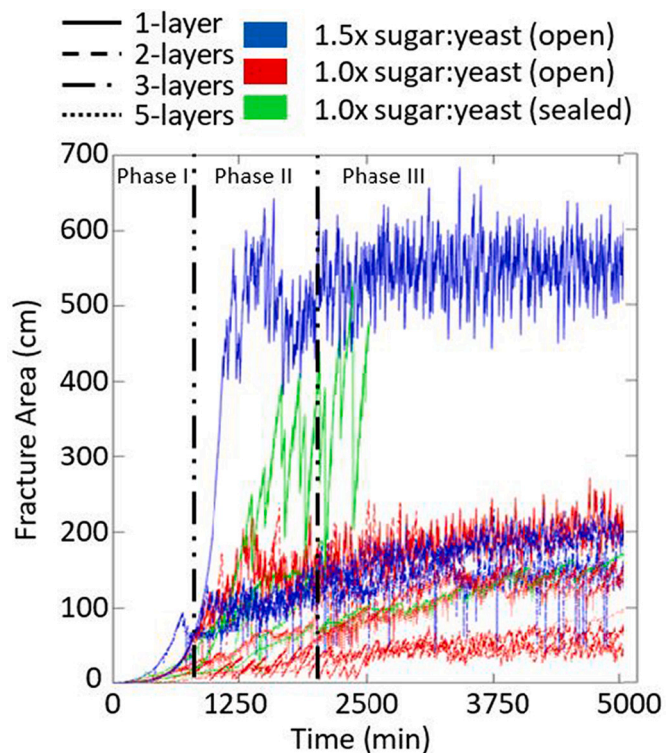
Fig. 11. Total surface area of microfracture aperture as a function of time. The intermittent expansion and contraction of the surface area in Phase III correlate to the opening and closing of microfractures as CO_2 is expelled from a fully developed network. Black vertical dash-dot-dot lines separate out approximately three phases discussed in the text: I (nucleation), II (microfracture growth), and III (intermittent closing and opening of the microfractures). See also Fig. 6.

existence of long-range elastic interactions. Conversely, the frequency independent correlation ($1/f^0$) indicates a poorly interconnected network, resulting in pulsations that are comparatively random. The power-law exponents vary between -1.74 and -0.28 (Fig. 12c). Experiments with 1-layer were closest to the reference line $1/f$ within their experiment class. Increasing the number of layers and introducing lateral sealing resulted in smaller power-law exponents (i.e., poorer connectivity).

Fluid flow relationships are tied to fracture topology that is effectively established by the end of Phase II (Figs. 9, 13). XYI-nodes are particularly helpful in understanding the relationship between the fracture network and ease of fluid flow. Fig. 13 shows the distribution of XYI-nodes on a ternary diagram. Utilizing Eq. 3, the parameter ε quantifies how well the fracture pattern may accommodate the fluid flow. Analysis of the distribution of XYI-nodes (Fig. 13) in relationship to ε reveals that a more interconnected network with a greater number of X- and Y-nodes results in higher permeability for the $1.5\times$ sugar:yeast concentration experiments. Sealed experiments are the next most permeable, with open $1.0\times$ sugar:yeast experiments being the least (Fig. 13).

The open experiments with $1.0\times$ sugar and yeast concentration plot below the line $\varepsilon = 2$. Sealed experiments plot on either side of the line $\varepsilon = 2$, indicating that the experiments generally are better connected, facilitating flow. Similarly, the $1.5\times$ sugar and yeast concentration experiments have significantly more X-nodes and plot below the line $\varepsilon = 3$. It is also worth noting that the 1-layer experiments always have the best potential flow rate (i.e., permeability) within an experiment class. Increasing the number of layers generally correlates to a decrease in potential flow rate within each experiment class.

Fig. 12. Fourier transform of the total surface area of microfracture aperture, (A(t), as a function of time and the characterization of intermittent fluid flow within the microfracture network for each experiment. a) Fourier transform showing the peak frequency of A(t). b) Same as a) on a double logarithmic scale to isolate the peak frequencies and their amplitudes. c) Fourier transform normalized by the peak frequency of each experiment in order to investigate the degree of microfracture interactions in each experiment type. Black dash-dot-dot lines indicate $1/f^2$, $1/f$, and a flat slope.
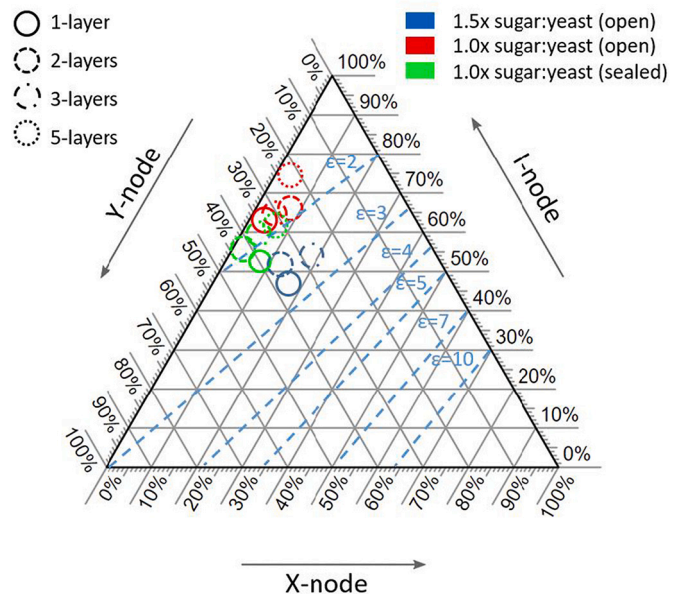
(Fig. 12b). Open experiments with a higher concentration of sugar:yeast ($1.5\times$) consistently had slightly greater peak frequency values, ranging from $10^{\text{to }2.79}$ to $10^{-2.77}$ Hz, corresponding to time scales in the range of 590–620 s (Fig. 12b). Finally, sealed experiments had even greater peak frequency values, ranging from $10^{\text{to }2.65}$ to $10^{-2.52}$ Hz, corresponding to time scales in the range of 330–450 s (Fig. 12b).

To obtain Fig. 12c, the curves in Fig. 12b were collapsed by normalizing the FFT by the position and amplitude of the peak. The non-linear dynamics of microfracture opening and closing are described by the slope of linear trends in the log-log plot, which correspond to power laws. Based on the work of Bons and van Milligen (2001), Kobchenko et al. (2014) established that $1/f^2$ describes the frequency evolution of a single fracture, while $1/f$ describes the frequency evolution of a well-connected fracture network that pulsates as a whole system due to the

Fig. 13. Ternary diagram representing the distribution (%) of XYI-nodes (Fig. 3c). The dashed blue lines correlate to hypothesized and later empirically established degrees of connectivity that influence the permeability of a given microfracture network, where $\varepsilon = 2$ is poorly connected, and $\varepsilon = 10$ is considered well connected (Sanderson and Nixon, 2015; Silva et al., 2021). Note, for natural systems, values of ε are dominantly in the range 2–4 (Sanderson and Nixon, 2015; Alvarez et al., 2021; Silva et al., 2021). (For interpretation of the references to color in this figure legend, the reader is referred to the web version of this article.)

5. Discussion

5.1. Comparison to previous experimental studies

The work presented here follows previous experimental studies completed by Kobchenko et al. (2013, 2014) and Vega and Kovscek (2019), who also studied organic-rich shale microfracturing by incorporating additional complexity found in natural systems. Similar to the goals of previous experiments (Kobchenko et al., 2013; Kobchenko et al., 2014; Vega and Kovscek, 2019), the focus was placed on small deformations due to elastic interactions related to the opening and closing of microfractures. This precludes the more elasto-plastic rheology of shale at a macro-scale. The 1-layer experiments are best representative of the isotropic plane within transversely isotropic rocks, including organic-rich shales at a finer scale (mm-cm) (Kobchenko et al., 2013; Kobchenko et al., 2014; Vega and Kovscek, 2019; Johnson et al., 2022b). Our experiments used a 1-layer model, including varying the concentration of sugar:yeast, to reproduce the results of these previous studies. Our results extend the data available on microfracture nucleation sites. We calculated the nucleation densities for the experimental data reported in Kobchenko et al. (2013) and found values of $0.41/cm^2$ and $0.55/cm^2$ compared to our value of $0.58/cm^2$. Vega and Kovscek (2019) utilized the $1.5\times$ sugar:yeast concentration for their experiments. They measured nucleation densities of $0.76/cm^2$, $1.16/cm^2$, $1.19/cm^2$, and $1.28/cm^2$ compared to $1.27/cm^2$ for our $1.5\times$ sugar:yeast 1-layer experiment. Therefore, the results in the present study show comparable values to previous experiments.

Kobchenko et al. (2014) and Vega and Kovscek (2019) observed that microfracture growth occurs in three stages, as is the case for the present study. During the initial stage, penny-shaped microfractures nucleate as CO_2 diffusion through the matrix fails to expel the gas quickly enough from the apparatus. This stage is followed by a period of rapid microfracture growth and further nucleation, wherein microfractures propagate from initial nucleation points. During this stage, in 1-layer experiments, the microfractures coalesce, ultimately creating a dominant connected microfracture network (Fig. 7), that may be assisted in draining the CO_2 by a series of smaller microfracture networks (Kobchenko et al., 2013; Kobchenko et al., 2014; Vega and Kovscek, 2019). Our experiments confirm this pattern for both the $1.0\times$ and $1.5\times$ sugar:yeast concentrations in the 1-layer experiments (Fig. 6). Furthermore, the final microfracture patterns appear similar to Kobchenko et al. (2013, 2014), which is also quantified by similar values of the parameter ω (Fig. 9). The average value of ω in the present study is 0.38, compared to 0.37 for Kobchenko et al. (2013). The microfracture patterns observed by Vega and Kovscek (2019) were more curvilinear. However, the values of the angle of coalescence between microfractures (Fig. 8) confirm the results previously established in all comparable studies (Kobchenko et al., 2013; Kobchenko et al., 2014).

In the final stage (i.e., Phase III), little to no microfracture growth occurs. However, the microfractures continue to open and close intermittently as the CO_2 is drained (Fig. 12, Phase III), as observed in previous studies (Kobchenko et al., 2014; Vega and Kovscek, 2019). This is represented by the periodic opening and closing of fractures (Fig. 11). Stronger periodicity is indicative of diffusion, while more irregular behavior as seen in Fig. 11 indicates a combination of fracture dominated flow alongside diffusion (de Reise et al., 2020). Kobchenko et al. (2014) noted that the drainage is defined by a characteristic frequency and non-linear behavior characterized by power laws. The peak frequency of microfractures opening and closing, which characterizes the fluid movement of the system within microfractures, varies depending on the concentration of sugar:yeast in the system (Fig. 12b). The power spectrum slope of $1/f$ for 1-layer experiments is confirmed with a value of -1.74 from Kobchenko et al. (2014) and a value of -1.69 for the present study. Kobchenko et al. (2014) noted that, while the dynamics of a single microfracture will have a slope of $1/f^2$, a slope of $1/f$ is representative of a connected microfracture system with good inter-

microfracture communication. The results of both Kobchenko et al. (2014) and the present study also show self-organized criticality (Bons and van Milligen, 2001).

Li et al. (2020) conducted a series of experiments using gelatin in 3D, where they investigated the behavior of an elastic medium during the microfracturing process. However, instead of internal fluid generation, red ink was injected in order to create a singular extensive microfracture to investigate hydraulic fracturing. Similar to other studies with gelatin (Kobchenko et al., 2013; Kobchenko et al., 2014; Vega and Kovscek, 2019; Li et al., 2020), the relationship between mechanical properties of gelatin (i.e., Young's modulus, Poisson's ratio) and temperature is highlighted. Orientation of microfracture propagation (i.e., horizontal or vertical) was controlled by applying a vertical force to encourage the growth of vertical microfractures. This is in line with what is known about how stress-regimes impact microfracture growth (Zoback, 2007). Therefore, for microfracture growth to occur, the pressure applied would need to be greater than the inherent strength of gelatin, in addition to the force applied. However, with the absence of anisotropy and the presence of only one microfracture front modelled utilizing Perkins-Kern-Nordgren (PKN) and Kristonouch-Geertsma-Daneshy (KGD) microfracture propagation models (Smith and Montgomoery, 2015; Li et al., 2020), it represents a single-porosity homogenous system (Heinemann and Mittermeir, 2012; Uzun et al., 2017; Johnson, 2018). The present study does not introduce a stress regime, and the base case has a complex microfracture network where all orientations are equally likely, as observed in previous studies (Kobchenko et al., 2013; Kobchenko et al., 2014; Vega and Kovscek, 2019). Nonetheless, all these studies are complementary to understanding hydraulic fracturing behavior. The introduction of anisotropy and a complex microfracture network is representative of dual-porosity systems commonly encountered during hydraulic fracturing in oil and gas reservoirs of all lithologies (Heinemann and Mittermeir, 2012; Smith and Montgomoery, 2015; Uzun et al., 2017; Johnson, 2018). Li et al. (2020) highlight the importance of a stress regime to artificial fracturing, while the present study reveals the importance of rock fabric as it impacts the propagation of microfractures. Furthermore, the present study could help evaluate how fracture topology will influence hydrocarbon extraction (Fig. 13).

5.2. Gas diffusion and nucleation of microfractures (phase I) in the context of primary migration

Gas diffusion is the dominant form of fluid expulsion prior to the onset of microfracturing (Kobchenko et al., 2013, 2014). This is confirmed by the $0.5\times$ sugar:yeast experiment (Table 1) that had CO_2 production without fracture nucleation. When diffusion is not sufficiently fast enough in expelling fluids compared to the CO_2 production rate, microfractures nucleate (Eq. 6). Increasing the sugar and yeast concentration increases the density of nucleation sites for microfractures. In the context of organic-rich shales during primary migration, this result indicates that increases in total organic carbon (TOC) content will have a comparatively greater impact on the number of nucleation points (i.e., kerogen lenses) that are activated. Modelling of organic-rich shales during kerogen conversion supports this supposition for shale with TOC between 0 and 8 wt% (Jin et al., 2010; Fan et al., 2010; Chauve et al., 2020). However, it has been established that, for Jurassic source rocks in the North Sea and the Barents Sea, TOC above ~8% does not result in a greater number of kerogen lenses (i.e., nucleation points) since the kerogen lenses begin to combine, resulting in a net decrease of the number of kerogen lenses per rock unit volume (Johnson et al., 2022b). The present study establishes that layering does not impact the number of nucleation points. This would suggest that all other factors being equal (i.e., kerogen type, chemical composition of lenses), a highly anisotropic shale (e.g., Hekkingen Formation, Vaca Muerta Formation, Wolfcamp Formation) with 2 wt% TOC would have just as many nucleation points as a shale with comparatively lower anisotropy (e.g., Bakken Formation, Green River Formation, Montney Formation) and

containing 2 wt% TOC.

Sealing the environment resulted in a ~ 36% drop in microfracture nucleation point density (Fig. 5) from an average of 0.45/cm^2 for the open experiments to 0.31/cm^2 for the partially sealed experiments. We suggest that the decrease in nucleation point density may correlate to a change in the ability for long range stress to be transferred within the system due to the presence of the partial seal (Eq. 4). Therefore, factors that influence the shale stress field (i.e., mineralogy, fluid) and loading stress may also impact the density of microfractures that nucleate during primary migration. The inhibition of new fractures in the vicinity of pre-existing microfractures may also influence the number and distribution of microfracture nucleation sites (Kobchenko et al., 2013).

5.3. Fracture growth and network interconnection (phase II) in the context of primary migration

In 1-layer (isotropic) open experiments, the angle of coalescence between two microfractures is usually high (i.e., >50°) by the end of Phase II (Fig. 6), similar to previous studies (Kobchenko et al., 2013; Kobchenko et al., 2014; Vega and Kovscek, 2019). In an isotropic environment, a microfracture tip deflection can occur when the maximum component of the stress tensor around a microfracture tip changes orientation such that the microfracture tip will bend towards a pre-existing microfracture (Takada, 1994; Watanabe et al., 2002). The introduction of anisotropy in the system, through varying the number of layers, has an effect on the angle of coalescence between two microfractures (Fig. 8; Table S1). This growth of microfractures parallel to layer boundaries can be seen in Fig. 7 more consistently for the 3-layers and 5-layers experiments than for the 1-layer and 2-layers experiments. Similar patterns have been observed in organic-rich shales during and after kerogen maturation (Kobchenko et al., 2011; Kalani et al., 2015; Ougier-Simonin et al., 2016; Johnson et al., 2022b). It is also worth noting that few microfractures propagate perpendicularly (i.e., vertically) between the layers (Fig. 7), connecting the largely parallel horizontal microfracture swarms in 3-layers and 5-layers experiments. This process has also been observed in nature and artificial maturation of organic-rich shales, wherein few vertical microfractures connect swarms of roughly horizontal (bedding parallel) microfractures (Kalani et al., 2015; Ougier-Simonin et al., 2016; Panahi et al., 2019; Johnson et al., 2022b).

The parameter ω has been used to characterize the topology of networks in isotropic and anisotropic media. For example, this parameter was used to study the statistical topology of river networks for more than 70 years (Horton, 1945; Wang et al., 2020). Rocks in the subsurface can contain well-developed anisotropic structures (e.g., shale, slates, gypsum, phyllites, schists, gneisses). Additionally, anisotropic rocks are generally isotropic in one direction and anisotropic in the other two directions (Kuila et al., 2011; Agliardi et al., 2014; Johnson et al., 2022b). Our experiments suggest that the microfracture network topology in isotropic rocks, or the isotropic direction of an anisotropic rock, is intermediate between a network that contains only isolated branches and an entirely fragmented network. Furthermore, the experiments indicate that a minimal number of layers (i.e., ~5) is required to shift microfracture interaction behavior to an almost entirely branching network (Fig. 9), as described by Eq. 10. This result would suggest that the way microfracture networks grow and interact with themselves is at least partially controlled by the fabric of the medium. The described pattern can be seen in organic-rich shales (Kobchenko et al., 2011; Ougier-Simonin et al., 2016; Johnson et al., 2022b).

Our experiments highlight that the likelihood of a microfracture breaking through a layer is dependent on the angle of intersection with that layer (Fig. 10). For an angle equal to or larger than 50°, a microfracture has a ~ 70% probability of breakthrough, while this probability drops to ~15% on average if the angle is below 50° (Fig. 9). When a microfracture fails to break through a layer, it may deflect along with the interface between the two layers (Figs. 3 and 10). Ghani et al. (2015)

developed numerical models to show that stronger seals will result in fracture deflection, while weaker seals will initially build up horizontal fractures that ultimately allow the progression of 'evenly' spaced vertical seals. While there are not enough fractures in our experiments to provide even spacing, the analogue model confirms a collection of horizontal fractures linked by a few vertical fractures (Fig. 7). Analysis of natural systems also show this observation (Vass et al., 2014; Koehn et al., 2020). In the laboratory, vertical microfracture breakthrough for angles larger than 50° has been shown to occur during the artificial maturation of organic-rich shales that were laterally sealed (Ougier-Simonin et al., 2016; Panahi et al., 2019). However, the introduction of sealing in our experiments favored microfracture growth that had a tendency to interact at an angle greater than 50° in the layered experiments (Fig. 10). Therefore, the development of microfractures that propagate perpendicular to layering may be the result of laboratory conditions in our experiments.

However, if all naturally occurring microfractures due to maturation within organic-rich shale were at a low angle (<30°) with respect to layering, the amount of interactions that typically occur would result in a certain number of microfractures penetrating each subsequent layer allowing for fluid migration across sedimentary layers. Johnson et al. (2022b) suggested that the initial angle of microfracture propagation will depend on the internal orientation of the kerogen lens, which can deviate ±30° from bedding, on average. Therefore, depending on the number of kerogen lenses present (Johnson et al., 2022b) and the degree of maturation (Zhao et al., 2016; Johnson et al., 2022a), high angle (i.e.,>50°) fracturing should not be required for hydrocarbon migration to occur.

5.4. Fluid migration (Phase III) in the context of primary migration

The relationship between fractures and fluid flow is well established (e.g., Heinemann and Mittermeir, 2012; Nolte and Nolte, 2015; Sanderson and Nixon, 2015; Uzun et al., 2017). XYI-node classification has been proposed as one possible tool to help understand this relationship (Sanderson and Nixon, 2015). Silva et al. (2021) established that media dominated by X- or Y- nodes are ~1000× more permeable than those dominated by I-nodes, while those with an equal distribution of all three are ~400× more permeable than those with solely I-nodes. Increasing layering (i.e., anisotropy) results in a less permeable fracture network (Figs. 7, 12, 13). Triaxial tests performed on shale and classified according to XYI-nodes confirm this result. As the stress regimes applied become more anisotropic, an increase in the number of I-nodes results in decreased permeability (He et al., 2021). The impact of fluid viscosity was also studied in the triaxial tests, suggesting that increasing fluid viscosity results in increased permeability (He et al., 2021). The present study did not introduce different viscosities for the fluid produced, but this is a variable present in primary migration (Jones, 1987; Vandenbroucke and Largeau, 2007). It was found that lower viscosity fluids resulted in greater network fracturing, interconnection, and higher permeability (He et al., 2021). Therefore, as viscosity increases with hydrocarbon chain complexity, all other variables being equal, shales with Type I kerogen (e.g., Barremian Bucomazi Formation, Vaca Muerta Formation) should form less permeable microfracture networks than those dominated by Type II kerogen (e.g., Bakken Formation, Kimmeridge Formation, Montney Formation, Wolfcamp Formation). Similarly, fracture networks in shale with Type III kerogen (e.g., Kimmeridge Formation, Wolfcamp Formation) will be more complex than that dominated by either Type I or Type II.

Beyond fracture topology, our experiments have established that higher TOC content will result in both faster and greater hydrocarbon production (Figs. 11, 12). Numerous studies confirm this result (Fan et al., 2010; Jin et al., 2010; Kobchenko et al., 2014; Kalani et al., 2015; Johnson, 2017; Teixeira et al., 2017; Chauve et al., 2020; Rabbel et al., 2020; Johnson et al., 2022b). Our study also shows that changes in the stress field that occurs due to the placement of the rubber o-ring result in

faster gas production (Fig. 12b), which has also been previously established (Heinemann and Mittermeir, 2012; Nolte and Nolte, 2015; Uzun et al., 2017). The experiments with a higher stress field also had greater periodicity, potentially suggesting diffusion is a greater factor for fluid flow within these systems (de Reise et al., 2020). It is, however, interesting to note that the experiments indicate that systems with a lower stress field have a poorer ability to transmit stress, and increased layering (i.e., anisotropy) will result in poorer fluid flow connection (Fig. 12c).

5.5. Applications to other subsurface systems

Organic-rich shales exhibit layering at the millimeter to centimeter scale, wherein some layers are organic-rich and others are organic-poor (Hoosen, 1747; Blatt and Tracy, 1996; Merrimen et al., 2003; Chauve et al., 2020; Johnson et al., 2022b). Numerical simulations and 3D microtomography imaging have revealed that microfractures will grow within and interact between these layers (Fan et al., 2010; Rabbel et al., 2020; Chauve et al., 2020; Johnson et al., 2022b). The focus of the present study is placed on such organic-rich shales in the context of primary migration at a fine scale (mm-cm), wherein the emphasis can be placed on brittle deformations that occur prior to larger plastic deformations often observed in shales and other rocks. However, the results of our experiments may find some relevance for a number of other subsurface systems, including the conversion of hydrous to anhydrous minerals (e.g., gypsum to basanite, smectite to illite), interlayered limestone, and mudstone at a larger scale (m-km), dehydration of serpentine rocks in subduction zones, fracture growth within layered rocks (e.g., slates, gypsum, phyllites, schists, gneisses), and within partial melts.

During Phase I, the experiments are representative of the conversion of hydrous to anhydrous minerals (e.g., smectite to illite). Specifically, the reduction of three to zero water layers in the transition of smectite to illite results in a substantial decrease in volume resulting in fluid expulsion (Vidal and Dubacq, 2009). This transition occurs in a similar PT regime to the conversion of kerogen lenses (Tissot et al., 1974; Vidal and Dubacq, 2009). The orientation of the long-axis of clay minerals, similar to that of kerogen lenses, is generally parallel to the layering (i.e., anisotropy) of the shale fabric (Vandenbroucke and Largeau, 2007; Johnson et al., 2022b). It has been proposed that fracturing will occur in line with the long-axis (Fan et al., 2010; Voltolini and Franklin, 2020; Johnson et al., 2022b) or pre-existing anisotropy, as seen in the present study (Fig. 7). Another form of anisotropy that has a similar impact on nucleation and initial fracture growth direction is the presence of a preferential stress direction (Fusseis et al., 2012; Rummel et al., 2020). During the conversion of gypsum to basanite, fracture growth will propagate parallel to the pre-existing anisotropy direction (Fusseis et al., 2012). Similarly, Rummel et al. (2020) have shown that alterations in stress direction have a significant impact on the direction of fracture growth.

Once microfractures begin to coalesce during Phase II, the fabric of the medium or layering (i.e., anisotropy) influences how microfracture networks grow and release fluids. Comparisons of relatively isotropic rocks or orientations of those rocks with anisotropic rocks or orientations reveal that fabric influences the angles of coalescence between fractures. Furthermore, the fabric influences the fracture topology of the networks. It has been noted that this is observable in organic-rich shales (Kobchenko et al., 2011; Ougier-Simonin et al., 2016; Johnson et al., 2022b), gypsum/basanite systems (Fusseis et al., 2012), and metamorphic schists and gneisses (Agliardi et al., 2014). Occasional microfractures that break through across layering have also been recorded in these same systems. The material properties of the fabric also influence microfracturing, wherein a layer of comparably higher strength will result in a greater number of microfractures deflecting while a layer of lower strength will result in comparatively few vertical fractures interconnected by many horizontal fractures (Ghani et al., 2015; Koehn et al.,

2020). This material property element, within anisotropy, was not directly investigated. However, it sits at the axis between anisotropy and sealing.

The influence of layering (i.e., anisotropy) and sealing has a significant impact on fracture topology and, by extension, fluid flow within layered rocks other than shale (e.g., slates, gneisses, schists). Our experiments indicate that higher levels of layering will result in poorer communication (Fig. 13). This is further complicated by variations in layer thickness (Rijken and Cooke, 2001) which can vary by a significant percentage in metamorphic rocks (Williams, 1990). Fractures transecting layers have greater success when they are thinner. This is well represented by the number of fractures that transect the inactive host of the 5-layer experiments as opposed to the 2-layer experiments (Fig. 7).

Crustal partial melt systems are usually anisotropic (e.g., stromatic migmatites), although it has not been fully established what structure partial melts may take in the mantle (Vigneresse and Clemens, 2000; Marchildon and Brown, 2003; Bons et al., 2009). Within the model of fractured networks, emplacement occurs through a fractured network system (Clemens and Droop, 1998), wherein the percolation rate is dependent on the drain rate (Vigneresse and Clemens, 2000; Bons et al., 2009). This mechanism of magma-emplacement may explain how the smallest fractures can feed larger dykes and, finally, plutons (Brown and Solar, 2009). Bons et al. (2009) suggested that the mechanism of magma emplacement would stop because of sealing, preventing stable connectivity as seen in the experiments (Fig. 7). Instead, melt accumulation would occur in a stepwise manner (Bons et al., 2009; Saukko et al., 2020). Other studies proposed a stable connection between melt accumulations (Brown and Solar, 1998; Sawyer, 2001; Vanderhaeghe, 2009). Xiong et al. (2019) modeled melt transport within a connected system that would be an apt comparison to the analogue models of the present study. Most models of melt transport exhibit some degree of self organization (Vanderhaeghe, 2009; Bons et al., 2009; Saukko et al., 2020), as displayed in Fig. 12. Should lateral sealing be present within these systems (Chakraborty, 2017; Rummel et al., 2020), it would have an impact on network communication, as seen within our experiments (Figs. 11–13). Critically the degree of connectivity, as modeled, may impact the rate of magma drainage.

6. Conclusions

Our analogue experiment explores the formation of microfractures in low permeability and layered brittle solids during internal fluid production. The presence of yeast and sugar that leads to the production of gaseous carbon dioxide controls fluid production in the solid. Three phases are observed within all experiments, starting with (1) an initial production of CO_2 resulting in the nucleation of penny-shaped microfractures, (2) followed by the growth of a microfracture network, and (3) finally, fluid expulsion resulting in intermittent microfractures opening and closing. This analogue system exhibits a rich dynamical behavior that provides a proxy for several natural processes in the Earth's crust in which fluid expulsion is controlled by both internal fluid production and elastic interactions.

The presence of layering (i.e., anisotropy) in the system has no influence on the nucleation density of microfractures. Furthermore, layering impedes and influences microfracture growth. Specifically, an increase in the number of microfractures parallel to the anisotropy direction results in more oblique angle intersections between microfractures. Increased layering also results in a more disconnected microfracture network resulting in poorer fluid communication.

The introduction of sealing potentially alters the ability for stress to be transmitted within the host matrix and reduces the nucleation density of microfractures. Despite fewer nucleation sites, the microfractures created showed a better connectivity even when anisotropy is introduced. This results in a greater number of microfractures intersecting layers at high angles ($>50°$), thereby ensuring greater breakthrough success. However, this change in the stress field also appears to have

impacted the rate of fluid production. Interestingly, the combination of layering with a poorer ability to transmit stress resulted in poorer fluid flow connection while maintaining a higher total rate of fluid production.

Applications of the study are particularly relevant when trying to understand organic-rich shales in the context of primary migration. Important parameters, including the impact of layering and changes in stress transmissibility (e.g., changes in mineralogy), are common and complex problems that apply to primary migration within organic-rich shales. The results of the experiments are also applicable to other natural processes (i.e., partial melts, conversion of hydrous minerals to anhydrous, fracturing in layered media).

Supplementary data to this article can be found online at https://doi.org/10.1016/j.tecto.2022.229575.

Declaration of Competing Interest

The authors declare that they have no known competing financial interests or personal relationships that could have appeared to influence the work reported in this paper.

Data availability

Data will be made available on request.

Acknowledgements

References

Agliardi, F., Zanchetta, S., Crosta, G.B., 2014. Fabric controls on the brittle failure of folded gneiss and schist. Tectonophysics 637, 150–162. https://doi.org/10.1016/j.tecto.2014.10.006.

Alvarez, L.L., Guimaraes, L.J.N., Gomes, I.F., Beserra, L., Pereira, L.C., Miranda, T.S., Maciel, B., Barbosa, J.A., 2021. Impact of fracture topology on the fluid flow behavior of naturally fractured reservoirs. Energies. 14, 5488. https://doi.org/10.3390/en14175488.

Anders, M.H., Laubach, S.E., Scholz, C.H., 2014. Microfractures: a review. J. Struct. Geol. 69, 377–394. https://doi.org/10.1016/j.jsg.2014.05.011.

Backeberg, N.R., Iavoviello, F., Rittner, M., Mitchell, T.M., Jones, A.P., Day, R., Wheeler, J., Shearing, P.R., Vermeesch, P., Striolo, A., 2017. Quantifying the anisotropy and tortuosity of permeable pathways in clay-rich mudstones using models based on X-ray tomography. Sci. Rep. 7, 14838. https://doi.org/10.1038/s41598-017-14810-1.

Bai, F.W., Anderson, W.A., Moo-Young, M., 2008. Ethanol fermentation technologies from sugar and starch feedstocks. Biotechnol. Adv. 26, 89–105. https://doi.org/10.1016/j.biotechadv.2007.09.002.

Bear, J., 1975. Dynamics of fluids in porous media. Soil Sci. 120 (2), 162–163. https://doi.org/10.1097/00010694-197508000-00022.

Beigbeder, J.B., Dantas, J.M.M., Lavoie, J.M., 2021. Optimization of yeast, sugar and nutrient concentrations for high ethanol production rate using industrial sugar beet molasses and response surface methodology. Fermentation 7, 86. https://doi.org/10.3390/fermentation7020086.

Blatt, H., Tracy, R.J., 1996. Petrology: Igneous, Sedimentary, and Metamorphic, 2nd ed.

Bons, P.D., van Milligen, B.P., 2001. New experiment to model self-organized critical transport and accumulation of melt and hydrocarbons from their source rocks. Geology 29 (10), 919–922. https://doi.org/10.1130/0091-7613(2001)029<0919:NETMSO>2.0.CO;2.

Bons, P.D., Dougherty-Page, J., Elburg, M.A., 2001. Stepwise accumulation and ascent of magmas. J. Metamorph. Geol. 19, 627–633. https://doi.org/10.1046/j.0263-4929.2001.00334.x.

Bons, P.D., Becker, J.K., Elburg, M.A., Urtson, K., 2009. Granite formation: stepwise accumulation of melt or connected networks? R. Soc. Edinburgh Trans. Earth Environ. Sci. 100, 105–115. https://doi.org/10.1017/S175569100901603X.

Bourdon, B., Turner, S., Dosseto, A., 2003. Dehydration and partial melting in subduction zones: Constraints from U-series disequilibria. J. Geophys. Res. 108 (B6), 2291. https://doi.org/10.1029/2002JB001839.

Brizzi, S., Funiciello, F., Corbi, F., Giuseppe, E.D., Mojoli, G., 2016. Salt matters: how salt affects the rheological and physical properties of gelatine for analogue modelling. Tectonophysics. 679, 88–101. https://doi.org/10.1016/j.tecto.2016.04.021.

Brown, M., Solar, G., 1998. Shear-zone systems and melts: feedback relations and self-organization in orogenic belts. J. Struct. Geol. 20 (2–3) 211–227. https://doi.org/10.1016/s0191-8141(97)00068-0.

Brown, M., Solar, G.S., 2009. Shear-zone systems and melts: feedback relations and self-organization in orogenic belts. J. Struct. Geol. 20 (2–3), 211–227. https://doi.org/10.1016/S0191-8141(97)00068-0.

Cardenes, V., Lopez-Sanchez, M.A., Barou, F., Olona, J., Llana-Funez, S., 2021. Crystallographic preferred orientation, seismic velocity and anisotropy in roofing slates. Tectonophysics. 808, 228815 https://doi.org/10.1016/j.tecto.2021.228815.

Chakraborty, S., 2017. A new mechanism for upper crustal fluid flow driven by solitary porosity waves in rigid reactive media? Geophys. Res. Lett. 44, 10324–10327. https://doi.org/10.1002/2017GL075798.

Chauve, T., Scholtès, L., Donzé, F., Mondol, N.H., Renard, F., 2020. Layering in shales controls microfracturing at the onset of primary migration in source rocks. J. Geophys. Res. Solid Earth 125. https://doi.org/10.1029/2020JB019444 e2020JB019444.

Clemens, J.D., Droop, G.T.R., 1998. Fluids, P–T paths and the fates of anatectic melts in the Earth's crust. Lithos 44 (1–2), 21–36. https://doi.org/10.1016/S0024-4937(98)00020-6.

Clemens, J.D., Mawer, C.K., 1992. Granitic magma transport by fracture propagation. Tectonophysics. 204 (3–4), 339–360. https://doi.org/10.1016/0040-1951(92)90316-X.

Coulomb, C.A., 1776. Essai sur une application des regles des maximis et minimis a quelquels problemesde statique relatifs, a la architecture. Mem. Acad. Div. Sav. 7, 343–387.

Craddock, P.R., Doan, T.V.L., Bake, K., Polyakov, M., Charsky, A.M., Pomerantz, A.E., 2015. Evolution of kerogen and bitumen during thermal maturation via semi-open pyrolysis investigated by infrared spectroscopy. Energy Fuel 29, 2197–2210. https://doi.org/10.1021/ef5027532.

Dahm, T., 2000. On the shape and velocity of fluid-filled fractures in the Earth. Geophys. J. 142 (1), 181–192. https://doi.org/10.1046/j.1365-246x.2000.00148.x.

Davies, J.H., 1999. The role of hydraulic fractures and intermediate-depth earthquakes in generating subduction-zone magmatism. Nature 398 (11), 142–145. https://www.nature.com/articles/18202.

de Reise, T., Bons, P.D., Gomez-Rivas, E., Sachau, T., 2020. Interaction between crustal-scale darcy and hydrofracture fluid transport: a numerical study. Geofluids. 8891801 https://doi.org/10.1155/2020/8891801.

Demaison, G., Huizinga, B.J., 1991. Genetic classification of petroleum systems. AAPG Bull. 75 (10), 1626–1643. https://doi.org/10.1306/0C9B29BB-1710-11D7-8645000102C1865D.

Fan, Z.Q., Jin, Z.H., Johnson, S.E., 2010. Subcritical propagation of an oi-filled penny-shaped crack during kerogen-oil conversion. Geophys. J. Int. 182, 1141–1147. https://doi.org/10.1111/j.1365-246X.2010.04689.x.

Fusseis, F., Schrank, C., Liu, J., Karrech, A., Llana-Funez, S., Xiao, X., Regenauer-Lieb, K., 2012. Pore formation during dehydration of a polycrystalline gypsum sample observed and quantified in a time-series synchrotron X-ray micro-tomography experiment. Solid Earth. 3, 71–86. https://doi.org/10.5194/se-3-71-2012.

Ghani, I., Koehn, D., Toussaint, R., Passchier, C.W., 2015. Dynamics of hydrofracturing and permeability evolution in layered reservoirs. Front. Phys. 3, 67. https://doi.org/10.3389/fphy.2015.00067.

Griffith, A.A., 1921. The phenomena of rupture and flow in solids. Philos. Trans. R. Soc. Lond. Ser. A Contain. Pap. Math. Phys. Character 221, 163–198. https://doi.org/10.1098/rsta.1921.0006.

He, Q., He, B., Li, F., Shi, A., Chen, J., Xie, L., Ning, W., 2021. Fractal characterization of complex hydraulic fractures in oil shales via topology. Energies. 14, 1123. https://doi.org/10.3390/en14041123.

Heinemann, Z.E., Mittermeir, G.M., 2012. Derivation of the Kazemi-Gilman-Elsharkawy generalized dual porosity shape factor. Transp. Porous Media 91, 123–132. https://doi.org/10.1007/s11242-011-9836-4.

Hendersen, C.M., Zeno, W.F., Lerno, L.A., Longo, M.L., Block, D.E., 2013. Fermentation temperature modulus phosphatidylethanolamine and phosphatidylinositol levels in the cell membrane of saccharomyces cerevisiae. Appl. Environ. Microbiol. 79 (17), 5345–5356. https://doi.org/10.1128/AEM.01144-13.

Hirschmann, M.M., Asimow, P.D., Ghiorso, M.S., Stolper, E.M., 1999. Calculation of peridotite partial melting from thermodynamic models of minerals and melts. III. Controls on isobaric melt production and the effect of water on melt production. J. Petrol. 40 (5), 831–851. https://doi.org/10.1093/petroj/40.5.831.

Hoosen, W., 1747. The Miner's Dictionary. Wrexham.

Horton, 1945. Erosional development of streams and their drainage basins; hydrophysical approach to quantitative morphology. GSA Bull. 56, 275–370. https://doi.org/10.1130/0016-7606(1945)56[275:EDOSAT]2.0.CO;2.

Jin, Z.H., Johnson, S.E., Fan, Z.Q., 2010. Subcritical propagation and coalescence of oil-filled cracks: getting the oil out of low-permeability source rocks. Geophys. Res. Lett. 37, L01305. https://doi.org/10.1029/2009GL041576.

Johnson, J.R., 2017. Applications of Geostatistical Seismic Inversion to the Vaca Muerta, Neuquen Basin, Argentina. Colorado School of Mines. M.Sc. Thesis. https://mountainscholar.org/bitstream/handle/11124/170976/Johnson_mines_0052N_11230.pdf?sequence=1.

Johnson, A.C., 2018. Constructing a Niobrara Reservoir Model Using Outcrop and Downhole Data. Colorado School of Mines. M.Sc. Thesis. https://mountainscholar.org/bitstream/handle/11124/172518/Johnson_mines_0052N_11579.pdf?sequence=1.

Johnson, J.R., Kobchenko Mondol, N.H., Renard, F., 2021. Analogue modelling of primary migration in shales using organic-rich and organic-poor layered gel. NGF Winter Conf. 34. https://geologi.no/images/NGWM20/Abstractvolume_NGWM20.pdf.

Johnson, J.R., Hansen, J.A., Rahman, J., Renard, F., Mondol, N.H., 2022a. Mapping the maturity of organic-rich shale with combined geochemical and geophysical data,

Draupne Formation, Norwegian Continental Shelf. Mar. Pet. Geol. 138, 105525 https://doi.org/10.1016/j.marpetgeo.2022.105525.

Johnson, J.R., Kobchenko, M., Mondol, N.H., Renard, F., 2022b. Multiscale synchrotron microtomography imaging of kerogen lenses in organic-rich shales from the Norwegian Continental Shelf. Int. J. Coal Geol. 103954 https://doi.org/10.1016/j.coal.2022.103954.

Jones, R.W., 1987. Organic Facies, advances in Petroleum Geochemistry, Brooks, J., Welte, D. Academic Press, London 2, 1–90.

Kalani, M., Jahren, J., Mondol, N.H., Faleide, J.I., 2015. Petrophysical implications of source rock microfracturing. Int. J. Coal Geol. 143, 43–67. https://doi.org/10.1016/j.coal.2015.03.009.

Kavanagh, J.L., Menand, T., Sparks, S.J., 2006. An experimental investigation of sill formation and propagation in layered elastic media. Earth Planet. Sci. Lett. 245, 799–813. https://doi.org/10.1016/j.epsl.2006.03.025.

Kavanagh, J.L., Menand, T., Daniels, K.A., 2013. Gelatine as a crustal analogue: determining elastic properties for modelling magmatic intrusions. Tectonophysics 582, 101–111. https://doi.org/10.1016/j.tecto.2012.09.032.

Kavanagh, J.L., Rogers, B.D., Boutelier, D., Cruden, A.R., 2017. Controls on sill and dyke-sill hybrid geometry and propagation in the crust: the role of fracture toughness. Tectonophysics. 698, 109–120. https://doi.org/10.1016/j.tecto.2016.12.027.

Kavanagh, J.L., Burns, A.J., Hazim, S.H., Wood, E.P., Martin, S.A., Hignett, S., 2018. Challenging dyke ascent models using novel laboratory experiments: implications for reinterpreting evidence of magma ascent and volcanism. J. Volcanol. Geotherm. Res. 354, 87–101. https://doi.org/10.1016/j.jvolgeores.2018.01.002.

Kobchenko, M., Panahi, H., Renard, F., Dysthe, D.K., Malthe-Sørenssen, A., Mazzini, A., Scheibert, J., Jamtveit, B., Meakin, P., 2011. 4D imaging of fracturing in organic-rich shaled during heating. J. Geophys. Res. 116, B12201. https://doi.org/10.1029/2011JB08565.

Kobchenko, M., Hafver, A., Jettestuen, E., Galland, O., Renard, F., Meakin, P., Jamtveit, B., Dysthe, D.K., 2013. Drainage fracture networks in elastic solids with internal fluid generation. Europhys. Lett. 102, 66002. https://doi.org/10.1209/0295-5075/102/66002.

Kobchenko, M., Hafver, A., Jettestuen, E., Renard, F., Galland, O., Jamtveit, B., Meakin, P., Dysthe, D.K., 2014. Evolution of a fracture network in an elastic medium with internal fluid generation and expulsion. Phys. Rev. 50, 052801 https://doi.org/10.1103/PhysRevE.90.052801.

Koehn, D., Piazolo, S., Sachau, T., Toussaint, R., 2020. Fracturing and porosity channeling in fluid overpressure zones in the shallow Earth's crust. Geofluids 7621759. https://doi.org/10.1155/2020/7621759.

Kuila, U., Dewhurst, D.N., Siggins, A.F., Raven, M.D., 2011. Stress anisotropy and velocity anisotropy in low porosity shale. Tectonophysics 503, 34–44. https://doi.org/10.1016/j.tecto.2010.09.023.

Li, S., Unsworth, M.J., Booker, J.R., Wei, W., Tan, H., Jones, A.G., 2003. Partial melt or aqueous fluid in the mid-crust of Southern Tibet? Constraints from INDEPTH magnetotelluric data. Geophys. J. Int. 153 (2), 289–304. https://doi.org/10.1046/j.1365-246X.2003.01850.x.

Li, Z., Wang, J., Gates, I.D., 2020. Fracturing gels as analogs to understand fracture behavior in shale gas reservoirs. Rock Mech. Rock. Eng. 53, 4345–4355. https://doi.org/10.1007/s00603-020-02153-9.

Lister, J.R., Kerr, R.C., 1991. Fluid-mechanical models of crack propagation and their application to magma transport in dykes. J. Geophys. Res. Solid Earth 96 (B6), 10049–10077. https://doi.org/10.1029/91JB00600.

Marchildon, N., Brown, M., 2003. Spatial distribution of melt-bearing structures in anatectic rocks from Southerm Brittany, France: implications for melt transfer at grain- to orogeny-scale. Tectonophysics. 364 (3–4), 215–235. https://doi.org/10.1016/S0040-1951(03)00061-1.

Matthew, A.S., Wang, J., Luo, J., Yau, S.T., 2015. Enhanced ethanol production via electrostatically accelerated fermentation of glucose using saccharomyces cerevisiae. Sci. Rep. 5, 15713. https://doi.org/10.1038/srep15713.

McKenzie, D., 1984. The generation and compaction of partially molten rock. J. Petrol. 25 (3), 713–765. https://doi.org/10.1093/petrology/25.3.713.

McKenzie, D., 1985. The extraction of magma from the crust and mantle. Earth Planet. Sci. Lett. 74 (1), 81–91. https://doi.org/10.1016/0012-821X(85)90168-2.

Merrimen, R.J., Highley, D.E., Cameron, D.G., 2003. Definiton and characteristics of very-fine grained sedimentary rocks: clay, mudstone, shale and slate. British Geological Surv. 3 (281N), 1–14. https://nora.nerc.ac.uk/id/eprint/527458/1/CR03281N.pdf.

Nolte, L.J.P., Nolte, D.D., 2015. Approaching a universal scaling relationship between fracture stiffness and fluid flow. Nat. Commun. 7, 10663. https://doi.org/10.1038/ncomms10663.

Nur, A., Byerlee, J.D., 1971. An exact effective stress law for elastic deformation of rock with fluids. J. Geophys. Res. 76 (26), 6414–6419. https://doi.org/10.1029/JB076i026p06414.

Ougier-Simonin, A., Renard, F., Boehm, C., Vidal-Gilbert, S., 2016. Microfracturing and microporosity in shales. Earth Sci. Rev. 162, 198–226. https://doi.org/10.1016/j.earscirev.2016.09.006.

Ozkaya, I., 1988. A simple analysis of oil-induced fracturing in sedimentary rocks. Mar. Pet. Geol. 5 (3), 293–297. https://doi.org/10.1016/0264-8172(88)90008-6.

Panahi, H., Kobchenko, M., Meakin, P., Dysthe, D.K., Renard, F., 2019. Fluid expulsion and microfracturing during the pyrolysis of an organic rich shale. Fuel. 235, 1–16. https://doi.org/10.1016/j.fuel.2018.07.069.

Parker, N.G., Povey, M.J.W., 2010. Ultrasonic study of the gelation of gelatin: phase diagram hysteresis and kinetics. Food Hydrocoll. 26 (1), 99–107. https://doi.org/10.1016/j.foodhyd.2011.04.016.

Petruzalek, M., Lokajicek, T., Svitek, T., 2019. Fracturing of migmatite: Influence of anisotropy. In: Rock Mechanics for Natural Resources and Infrastructure Development, 1st ed. CRC Press.

Rabbel, O., Mair, K., Galland, O., Gruhser, C., Meier, T., 2020. Numerical modeling of fracture network evolution in organic-rich shale with rapid internal fluid generation. J. Geophys. Res. Solid Earth 125. https://doi.org/10.1029/2020JB019445 e2020JB019445.

Rijken, P., Cooke, M.L., 2001. Role of shale thickness on vertical connectivity of fractures: application of crack-bridging theory to the Austin Chalk, Texas. Tectonophysics 337, 117–133. https://doi.org/10.1016/S0040-1951(01)00107-X.

Rivalta, E., Bottinger, M., Dahm, T., 2005. Buoyancy-driven fracture ascent: experiments in layered gelatine. J. Volcanol. Geotherm. Res. 144 (1–4), 273–285. https://doi.org/10.1016/j.jvolgeores.2004.11.030.

Rivalta, E., Taisne, B., Bunger, A.P., Katz, R.F., 2015. A review of mechanical models of dike propagation: schools of thought, results and future directions. Tectonophysics 638, 1–42. https://doi.org/10.1016/j.tecto.2014.10.003.

Romero-Sarmiento, M.F., Euzen, T., Rohais, S., Jiang, C., Littke, R., 2016. Artificial thermal maturation of source rocks at different thermal maturity levels: Application to the Triassic Montney and Doig Formations in the Western Canada Sedimentary Basin. Org. Geochem. 97 (2016), 148–162. https://doi.org/10.1016/j.orggeochem.2016.05.002.

Rummel, L., Kaus, B.J.P., Baumann, T.S., White, R.W., Riel, N., 2020. Insights into the compositional evolution of crustal magmatic systems from coupled petrological-geodynamical models, 61(2), p. egaa029. https://doi.org/10.1093/petrology/egaa02961.

Sanderson, D.J., Nixon, C.W., 2015. The use of topology in fracture network characterization. J. Struct. Geol. 72 (2015), 55–56. https://doi.org/10.1016/j.jsg.2015.01.005.

Saukko, A., Ahlang, C., Nikkila, K., Soesoo, A., Eklund, O., 2020. Double power-law leucosome width distribution: implications for recognizing melt movement in migmatites. Front. Earth Sci. 8, 591871 https://doi.org/10.3389/feart.2020.591871.

Sawyer, E.W., 2001. Melt segregation in the continental crust: distribution and movement of melt in anatectic rocks. J. Metamorph. Geol. 19 (3), 291–309. https://doi.org/10.1046/j.0263-4929.2000.00312.x.

Sayers, C., 1999. Stress-dependent seismic anisotropy of shales. Geophysics. 64 (1), 93–98. https://doi.org/10.1190/1.1444535.

Secor, D.T., 1965. Role of fluid pressure in jointing. Am. J. Sci. 263, 633–646. https://doi.org/10.2475/ajs.263.8.633.

Secor, D.T., Pollard, D.D., 1975. On the stability of open hydraulic fractures in the Earth's crust. Geophys. Res. Lett. 2 (11), 510–513. https://doi.org/10.1029/GL002i011p00510.

Sili, G., Urbani, S., Acocella, V., 2019. What controls sill formation: an overview from analogue models. J. Geophys. Res. Solid Earth 124, 8205–8222. https://doi.org/10.1029/2018JB017005.

Silva, J.P., Gomes, I.F., Santos, R.F.V.C., Mirand, T.S., Guedes, R.P., Barbosa, J.A., Guimaraes, E.X., Beserra, L.B., Guimaraes, L.J.N., 2021. Topological analysis of fracture networks integrated with flow simulation models for equivalent fracture permeability estimation. J. Struct. Geol. 147, 104338 https://doi.org/10.1016/j.jsg.2021.104338.

Smith, M.B., Montgomoery, C., 2015. Hydraulic Fracturing. CRC Press. https://doi.org/10.1201/b16287.

Sorbadere, F., Laurenz, V., Frost, D.J., Wenz, M., Rosenthal, A., McCammon, C., Rivard, C., 2018. The behaviour of ferric iron during martial melting of peridotite. Geochemica et Cosmochimica Acta. 239 (2018), 235–254. https://doi.org/10.1016/j.gca.2018.07.019.

Takada, A., 1989. Magma transport and reservoir formation by a system of propagating cracks. Bull. Volcanol. 52, 118–126. https://doi.org/10.1007/BF00301551.

Takada, A., 1994. Accumulation of magma in space and time by crack interaction. International Geophysics. 57 (1994), 241–257. https://doi.org/10.1016/S0074-6142(09)60099-1.

Takei, Y., 2017. Effects of partial melting on seismic velocity and attenuation: a new insight from experiments. Annu. Rev. Earth Planet. Sci. 45, 447–470. https://doi.org/10.1146/annurev-earth-063016-015820.

Teixeira, M.G., Donze, F., Renard, F., Panahi, H., Papachristos, E., Scholtes, L., 2017. Microfracturing during primary migration in shales. Tectonophysics 694, 268–279. https://doi.org/10.1016/j.tecto.2016.11.010.

Tissot, B., Durand, B., Espitalie, J., Combaz, A., 1974. Influence of nature and diagenesis of organic matter in formation of petroleum. AAPG Bull. 58 (3), 499–506.

Uzun, I., Eker, E., Cho, Y., Kazemi, H., Rudledge, J.M., 2017. Assessment of rate transient analysis techniques for multiphase flow in unconventional reservoirs: applications to the Eagleford formation. In: SPE Western Regional Meeting. SPE-185737-MS. https://doi.org/10.2118/185737-MS.

Van Otterloo, J., Cruden, A.R., 2016. Rheology of pig skin gelatine: defining the elastic domain and its thermal and mechanical properties for geological analogue experiment applications. Tectonophysics 638, 86–97. https://doi.org/10.1016/j.tecto.2016.06.019.

Vandenbroucke, M., Largeau, C., 2007. Kerogen origin, evolution, and structure. Org. Geochem. 38, 719–833. https://doi.org/10.1016/j.orggeochem.2007.01.001.

Vanderhaeghe, O., 2009. Migmatites, granites and orogeny: flow modes of partially-molten rocks and magmas associated with melt/solid segregation in orogenic belts. Tectonophysics 477 (3–4), 119–134. https://doi.org/10.1016/j.tecto.2009.06.021.

Vass, A., Koehn, D., Ghani, I., Piazolo, S., Toussaint, R., 2014. The importance of fracture-healing on the deformation of fluid-filled layered systems. J. Struct. Geol. 67, 94–106. https://doi.org/10.1016/j.jsg.2014.07.007.

Vega, B., Kovscek, A.R., 2019. A systematic study of internal gas generation in shale source rocks using analog experiments. J. Pet. Sci. Eng. 173, 2019–2221. https://doi.org/10.1016/j.petrol.2018.10.006.

Vernik, L., Liu, X., 1997. Velocity anisotropy in shales: a petrophysical study. Geophysics. 62 (2), 521–532. https://doi.org/10.1190/1.1444162.

Vidal, O., Dubacq, B., 2009. Thermodynamic modelling of clay dehydration, stability and compositional evolution with temperature, pressure and H2O activity. Geochim. Cosmochim. Acta 73, 6544–6564. https://doi.org/10.1016/j.gca.2009.07.035.

Vigneresse, J.L., Clemens, J.D., 2000. Granitic magma ascent and emplacement: neither diapirism nor neutral buoyancy. Geol. Soc. Lond. Spec. Publ. 174 (1), 1. https://doi.org/10.1144/GSL.SP.1999.174.01.01.

Voltolini, M., Franklin, J.G.A., 2020. The sealing mechanisms of a fracture in Opalinus clay as revealed by in situ synchrotron X-Ray Micro-tomography. Front. Earth Sci. 8, 1–13. https://doi.org/10.3389/feart/2020.00207.

Wang, K., Yan, D., Qin, T., Weng, B., Wang, H., Bi, W., Li, X., Dorjsuren, B., 2020. A new topological and hierarchicical river coding method based on the hydroglogy structure. J. Hydrol. 580, 124243 https://doi.org/10.1016/j.jhydrol.2019.124243.

Watanabe, T., Masuyama, T., Nagaoka, K., Tahara, T., 2002. Analog experiments on magma-filled cracks: competition between external stresses and internal pressure. Earth, Planets, and Space. 54, 1247–1261. https://doi.org/10.1186/BF03352453.

Williams, P.F., 1990. Differentiate layering in metamorphic rocks. Earth Sci. Rev. 29 (1–4), 267–281. https://doi.org/10.1016/0012-8252(0)90042-T.

Xiong, Y., Zuo, R., Clarke, K.C., 2019. A fractal model of granitic intrusion and variability based on cellular automata. Comput. Geosci. 129, 40–48. https://doi.org/10.1016/j.cageo.2019.05.002.

Zhao, L., Qin, X., Han, D.H., Geng, J., Yang, Z., Cao, H., 2016. Rock-physics modeling for the elastic properties of organic shale at different maturity stages. Geophysics 81 (5), 527–541. https://doi.org/10.1190/GEO2015-0713.1.

Zhu, W., Gaetini, G.A., Fusseis, F., Montesi, L.G.J., Carlo, F.D., 2011. Microtomography of partially molten rocks: three-dimensional melt distribution in mantle peridotite. Science 232 (6025), 88–91. https://doi.org/10.1126/science.1202221.

Zoback, M., 2007. Reservoir Geomechanics. Cambridge University Press. https://doi.org/10.1017/CBO9780511586477.